Hysteresis parameters and magnetic anisotropy of silicate-hosted magnetite exsolutions

Even S. Nikolaisen [ORCID],[1] Richard Harrison,[1,2] Karl Fabian [ORCID],[1] Nathan Church [ORCID],[1] Suzanne A. McEnroe [ORCID],[1] Bjørn Eske Sørensen [ORCID][1] and Christian Tegner [ORCID][3]

[1]*Norwegian University of Science and Technology (NTNU), S. P. Andersens veg 15a, 7031 Trondheim, Norway. E-mail: even.nikolaisen@ntnu.no*
[2]*Department of Earth Sciences, University of Cambridge, Downing Street, Cambridge CB23EQ, UK*
[3]*Department of Geoscience, Aarhus University, Høegh-Guldbergs Gade 2, 8000 Aarhus, Denmark*

SUMMARY

Anisotropy of remanent magnetization and magnetic susceptibility are highly sensitive and important indicators of geological processes which are largely controlled by mineralogical parameters of the ferrimagnetic fraction in rocks. To provide new physical insight into the complex interaction between magnetization structure, shape, and crystallographic relations, we here analyse 'slice-and-view' focused-ion-beam (FIB) nano-tomography data with micromagnetic modelling and single crystal hysteresis measurements. The data sets consist of 68 magnetite inclusions in orthopyroxene (Mg_{60}) and 234 magnetite inclusions in plagioclase (An_{63}) were obtained on mineral separates from the Rustenburg Layered Suite of the Bushveld Intrusive Complex, South Africa. Electron backscatter diffraction was used to determine the orientation of the magnetite inclusions relative to the crystallographic directions of their silicate hosts. Hysteresis loops were calculated using the finite-element micromagnetics code MERRILL for each particle in 20 equidistributed field directions and compared with corresponding hysteresis loops measured using a vibrating sample magnetometer (VSM) on silicate mineral separates from the same samples. In plagioclase the ratio of remanent magnetization to saturation magnetization (M_{rs}/M_s) for both model and measurement agree within 1.0 per cent, whereas the coercivity (H_c) of the average modelled curve is 20 mT lower than the measured value of 60 mT indicating the presence of additional sources of high coercivity in the bulk sample. The VSM hysteresis measurements of the orthopyroxene were dominated by multidomain (MD) magnetite, whereas the FIB location was chosen to avoid MD particles and thus contains only particles with diameters <500 nm that are considered to be the most important carriers of palaeomagnetic remanence. To correct for this sampling bias, measured MD hysteresis loops from synthetic and natural magnetites were combined with the average hysteresis loop from the MERRILL models of the FIB region. The result shows that while the modelled small-particle fraction only explains 6 per cent of the best fit to the measured VSM hysteresis loop, it contributes 28 per cent of the remanent magnetization. The modelled direction of maximal M_{rs}/M_s in plagioclase is subparallel to $[001]_{plag}$, whereas H_c does not show a strong orientation dependence. The easy axis of magnetic remanence is in the direction of the magnetite population normal to $(150)_{plag}$ and the maximum calculated susceptibility (χ^*) is parallel to $[010]_{plag}$. For orthopyroxene, the maximum M_{rs}/M_s, maximum χ^* and the easy axis of remanence is strongly correlated to the elongation axes of magnetite in the $[001]_{opx}$ direction. The maximum H_c is oriented along $[100]_{opx}$ and parallel to the minimum χ^*, which reflects larger vortex nucleation fields when the applied field direction approaches the short axis. The maximum H_c is therefore orthogonal to the maximum M_{rs}/M_s, controlled by axis-aligned metastable single-domain states at zero field. The results emphasize that the nature of anisotropy in natural magnetite does not just depend on the particle orientations, but on the presence of different stable and metastable domain states, and the mechanism of magnetic switching between them. Magnetic modelling of natural magnetic particles is therefore a vital

method to extract and process anisotropic hysteresis parameters directly from the primary remanence carriers.

Key words: Magnetic fabrics and anisotropy; Magnetic mineralogy and petrology; Rock and mineral magnetism; Numerical modelling; Microstructures.

1 INTRODUCTION

The Rustenburg Layered Suite of the Bushveld Intrusive Complex, South Africa is a 2055–2056 Ma (Scoates *et al.* 2021) layered intrusion covering an area of 65 000 km^2 and a maximum thickness of 7 km (Cawthorn *et al.* 2016), making it the largest and oldest known layered intrusion. Layered intrusions are distinguishable by sharp vertical differences between gravitationally segregated silicates, formed by crystal fractionation and settling of minerals in layers on the chamber floor. Geological maps (Wager & Brown 1967) show the layered intrusive part of Bushveld Complex outcropping in four separate surface locations, the northern, western, southeastern and eastern lobes (Letts *et al.* 2009). These are internally connected and display distinct chemical similarities between their upper halves (Cawthorn *et al.* 1998; Webb *et al.* 2011). The extensively studied Bushveld intrusion is considered a primary location for understanding the magmatic processes of deep seated magma chambers. Research interest is fuelled by the economic enrichment of platinum group elements (PGE) that makes Bushveld the world's largest source of Pt and Pd mined every year (Crowson 2001; Thormann *et al.* 2017).

Palaeomagnetic studies (Hattingh 1986; Feinberg *et al.* 2006) describe gabbronorites and anorthosites in the main zone of the Bushveld intrusion as displaying some of the most stable magnetic remanence properties encountered in ancient rocks (Feinberg *et al.* 2006). This stable remanence is associated with magnetite that forms as exsolved or included particles in silicates like plagioclase (Davis 1981; Sobolev 1990; Feinberg *et al.* 2005; Usui *et al.* 2015) and pyroxene (Fleet *et al.* 1980; Renne *et al.* 2002; Frandsen *et al.* 2004; Feinberg *et al.* 2004) both within the Bushveld complex and in a wide range of other geologic settings. These magnetite inclusions often occur as several micrometer long rods in multiple crystallographically defined directions. Given their common occurrence in nature, and their potential to carry reliable palaeomagnetic information from ancient rocks (Bono *et al.* 2019), there is considerable interest in understanding the magnetic domain states of such inclusions (Nikolaisen *et al.* 2020) and the intrinsic magnetic anisotropy that arises from their non-random orientation distribution at the single-crystal scale. This anisotropy is of particular relevance when interpreting palaeomagnetic measurements from single-crystal samples (Bono *et al.* 2019), as it has the potential to modify the relationship between the direction and intensity of palaeomagnetic remanence and the ancient magnetizing field. More broadly, there is a fundamental need to understand the origin of anisotropy at the single-crystal scale, in order to relate bulk anisotropy measurements of igneous rocks to the mineralogical textures imparted by deformation and tectonic strain (Burton-Johnson *et al.* 2019). Here we explore the physical origins of magnetic anisotropy from first principles using a combination of focused-ion-beam (FIB) 'slice-and-view' nanotomography and finite-element micromagnetic simulations. We show that the nature of the anisotropy depends not only on the orientation distribution of the magnetite rods, but also on the presence of different stable and metastable domain states and the mechanism of magnetic switching between them.

2 MATERIALS AND METHODS

We here apply the general 'slice-and-view' method for extracting data, processing the resulting image stack, and calculating micromagnetic models as it is described step-by-step in Nikolaisen *et al.* (2020). For this study only few modifications to the method were introduced to increase the quality and accuracy of the results. Below only these changes are explained in sufficient detail to allow replication. All other details are described in Nikolaisen *et al.* (2020).

The most direct properties to compare modelled and measured data are the bulk average magnetic hysteresis parameters, M_s, saturation remanent magnetization M_{rs}, coercivity H_c and coercivity of remanence H_{cr}. In a bulk sample these properties are averaged over large particle ensembles that are usually randomly oriented in space, unless a lattice preferred orientation was generated during rock formation or later deformation. Each modelled curve represents a single field direction for a single particle, and the model results need to be averaged over both the particle ensemble and a sufficient number of field directions to compare them to the bulk measurements.

By this method it is possible to replicate equivalent hysteresis measurements based on FIB nanotomography and micromagnetic modelling (Nikolaisen *et al.* 2020). Because the hysteresis curves for each particle is modelled for equidistributed external field directions, all magnetic hysteresis results can also be averaged for each individual direction over the whole particle ensemble, and then provide additional information about their magnetic anisotropy. The general method used to magnetically model hysteresis loops for a natural assemblage of magnetite from FIB nanotomography is documented in Nikolaisen *et al.* (2020). Because these modelling results represent single silicate crystal hysteresis loops, they are here directly compared to VSM measurements of the corresponding silicate separates, even though these measurements represent much larger volumes. In addition, the modelled loops average only over smaller particle sizes which are within the FIB volume and can be modelled within a reasonable time. Therefore particles with an equivalent volume sphere diameter (EVSD) of >500 μm are excluded from the model.

2.1 Sample

The Rustenburg Layered Suite is subdivided into five zones, the Marginal (MZ), Lower (LZ), Critical (CZ), Main (MZ) and Upper (UZ). The B-16 specimen used in this study was collected on the Roossenekal Main Zone profile of the Bushveld eastern lobe 145 m below the pyroxenite marker (Lundgaard *et al.* 2006; Cawthorn *et al.* 2016). Sample B-16 was chosen because magnetite is its dominant magnetic mineral composition and there are both plagioclase and pyroxene separates available allowing individual single crystal hysteresis loops to be measured. Bulk NRM and bulk magnetic susceptibility value are volume normalized and measured to 6.4 A m^{-1} and 0.007 (SI), respectively for B-16 specifically. Petrographic analysis (Cawthorn *et al.* 2016) characterizes these samples as fine-grained gabbro norites with magnetite as the main opaque mineralization, appearing as an exsolved phase in both plagioclase

Table 1. Plagioclase and orthopyxene compositions for sample B16 of the Bushveld Complex. Data compiled from Lundgaard *et al.* (2006) and Cawthorn *et al.* (2016). Methods are described in Lundgaard (2003) and Lundgaard *et al.* (2006).

Mineral Method	Plagioclase XRF (bulk separate)	Plagioclase EMPA∗	Orthopyroxene EMPA∗∗
Major element compositions (wt. per cent)			
SiO_2	52.86	52.21	52.25
TiO_2	0.04		0.15
Al_2O_3	29.14	28.79	0.76
Cr_2O_3			0.06
Fe_2O_3	0.24		0.98
FeO	0.50	0.52	23.63
MnO	0.1		0.52
MgO	0.27		20.82
CaO	12.26	12.38	1.01
Na_2O	4.40	4.09	0.015
K_2O	0.27	0.28	
P_2O_5	0.01		
LOI	0.16		
Sum	100.16	98.28	100.19
An per cent	60.6	62.6 ± 0.9	
FeO_{tot}	0.71		24.51
Mg#			60.2 ± 0.2
Trace element compositions by ICPMS (ppm)			
Sr	507.93		
Ba	100.21		

∗5 μm beam ∗∗2 μm beam.

and pyroxene. The incorporation of iron into the silicates was a primary liquidus process during the crystallization for plagioclase (Tegner & Cawthorn 2010) and for pyroxene suggested to occur at primary subsolidus mineral formation, with magnetite exsolving at temperatures in the range of 600 °C (Fleet *et al.* 1980) to 865 °C (Feinberg *et al.* 2004).

Plagioclase is labradorite ($An_{62.6 \pm 0.9}$) (Lundgaard 2003; Cawthorn *et al.* 2016), comprising elongated crystals up to to 1.5 mm in length with albite twins parallel to the direction of elongation. Some sections of the plagioclase show symplectite and inclusions of quartz. Fe-oxides are found as inclusions in multiple crystallographic orientations (Fig. A5). The composition of plagioclase was determined both *in situ* (electron microprobe measurements with a 5 μm) and on the separated material (XRF measurements) at Aarhus University, Denmark. The two methods yield very similar results (Table 1), demonstrating that the plagioclase separate analysed in this study is very pure. The total iron content (FeO_{tot}) is 0.52 wt per cent for the in situ measurements and 0.71 wt per cent for the bulk separate. The higher FeO_{tot} in the bulk separate may indicate that tiny amounts of oxide or pyroxene were included in this material. Alternatively, it indicates that the *in situ* measurements did not include exsolved magnetite inclusions. Pyroxene is mainly orthopyroxene ($Mg_{60.2 \pm 0.2}$) with clinopyroxenene occurring as larger discrete grains (labelled as Cpx in Fig. A3). The orthopyroxene again show exsolution lamellae of inverted pigeonite (In-Pig in Fig. A3). The composition of orthopyroxene was determined with a focused beam (*ca.* 2 μm, Table 1). Clinopyroxene contains orthopyroxene exsolution lamellae with spinel. Fe-oxides hosted by the pyroxenes are observed in multiple relations. The largest occur as discrete grains of multidomain magnetite (300–500 μm) with oxy-exsolution of ilmenite lamellae and spinel (larger opaque grains in Fig. 1a). Within the orthopyroxene, there are multidomain magnetite (50–100 μm) inclusions with oxy-exsolved ilmenite lamellae [Fig. A3 (Mag 1) and Fig. A2c] oriented parallel to the inverted pigeonite lamellae. Occurring in local patches are magnetite exsolution lamellae [Figs A3 and A4 (Mag 2)] in orthopyroxene that range between 0.2 and 20 μm wide and typically <200 nm thick. Fig A4 shows these magnetites to be in contact with thinner (<200 nm) inverted pigeonite lamellae. Whenever the exsolved inverted pigeonite lamellae are wider, the magnetites are also observed to be larger and oriented normal to the magnetite exsolved in orthopyroxene (Fig. A4). Since we observe oxy-exsolved ilmenite in the larger magnetite inclusions, it is reasonable to assume that the magnetite lamellae in the pyroxene also contain ilmenite exsolution. While their small size makes it difficult to conclude, EDS does indicate trace values <1 wt. per cent Ti scattered in these magnetite lamellae. Unblocking temperatures measured by Letts *et al.* (2009) between 565 and 580 °C from similar samples in the eastern lobe Main Zone, suggest the main magnetic remanence carrier is low-Ti titanomagnetite or pure magnetite. Elsewhere in the pyroxene there are Fe-oxides that fill in cracks and at grain boundaries (Fig. A2a and labelled Fe-oxide in Fig. A3).

2.2 Slice-and-view

Raw data collection was performed using the Auto Slice & View 4 software on an FEI Helios G4 UX Dual-Beam Focused-Ion-Beam (FIB) microscope at the NTNU NanoLab in Trondheim, Norway. The beam drift issues described by Nikolaisen *et al.* (2020) were reduced by avoiding magnifications higher than 2500×. Electron-beam imaging was performed using a through-lens detector (TLD) for the Backscattered-Electron (BSE) signal in immersion mode at 3 kV and 0.4 nA. The milled volume from the plagioclase measures 27.93 μm × 16.1 μm × 12.84 μm (FIB_X-axis × FIB_Y-axis × FIB_Z-axis, Fig. 2). This volume was reconstructed from 643 slices, with a slice thickness of 20 nm. Each slice is a 1443 × 894 image with horizontal pixel size of 20.6 nm. For the pyroxene the milled volume measures 25.71 μm × 14.31 μm × 6.32 μm (FIB_X-axis × FIB_Y-axis × FIB_Z-axis) (Fig. 3), reconstructed from 317 slices with a slice thickness of 20 nm. Each slice is a 2113×1166 image with horizontal pixel size of 14.2 nm.

2.3 Image processing

After stacking and aligning the raster images of the milled front faces, the individual slices were corrected to remove the shadow effect caused by the angle between the milled front face and e-beam. The darkening of the lower part of each slice due to this shadowing was removed by calculating the Z average of the entire stack. This Z-average image predominantly reflects the voluminous host silicate and the instrumental shadowing, but also contains noise as well as brighter regions from areas where oxides persist over multiple slices. Therefore, a 2-D polynomial surface was fitted to the Z-average image and this surface is subtracted from each slice. Noise removal and smoothing was performed using a non-local means denoising Fiji plugin (Darbon *et al.* 2008; Buades *et al.* 2011). Tilt correction for the 52° angle between the ion- and electron-beam within the FEI software was unavailable for these samples and correction was done when recalculating pixel height (H) in Paraview with $H_{corrected} = H_{Projected}/\sin 52°$. Further processing to generate each particle as a stereolithographic (STL) file an solidifying the meshes follows the exact process in section 2.4 from Nikolaisen *et al.* (2020).
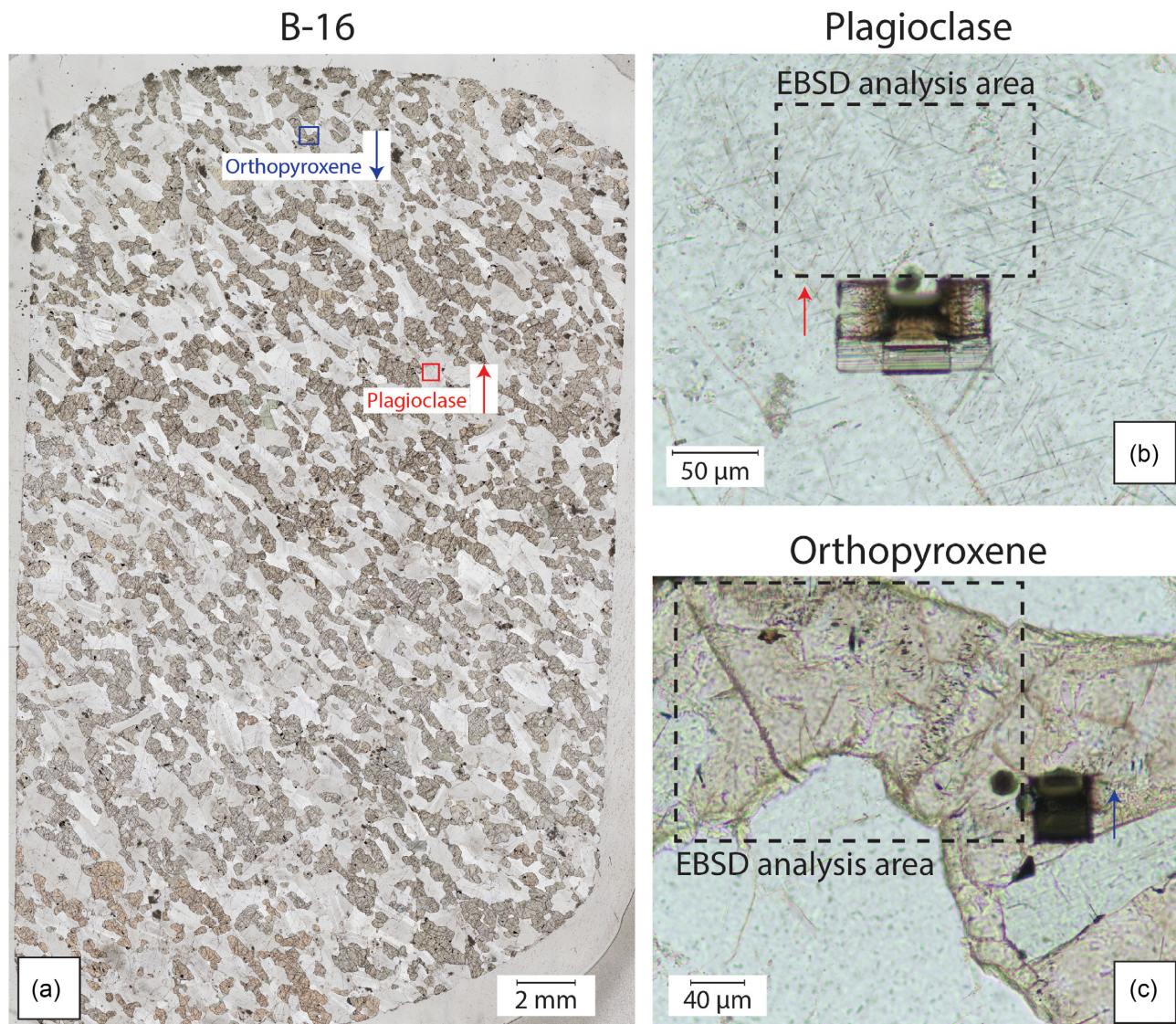
Figure 1. Optical plane polarized light scan of the B-16 thin section (a) showing the milling location in the plagioclase (b) and orthopyroxene (c). The red (plagioclase) and blue arrows (orthopyroxene) indicate the respective milling directions (FIB_{-Z}-axis in Figs 2 and 3). Note that the image in (c) is reversed with respect to (a). The black dashed boxes are the area analysed by EBSD.

2.4 Particle parameters

Particle dimensions and orientations were calculated from the individual particle STL file through the two python packages numpy-stl and trimesh (Dawson-Haggerty *et al.* 2019). A particles direction is represented by the orientation of the elongation axis, calculated by the Eigen matrix of the inertia tensor. Dimensions were extracted by calculating the minimum volume bounding box.

2.5 Micromagnetic modelling

Micromagnetic modelling uses the finite element code MERRILL (Ó Conbhuí *et al.* 2018; Fabian & Shcherbakov 2018). Each particle's initial remanent domain state was determined by minimizing the total micromagnetic energy from a starting state of fully randomized spins. While Nikolaisen *et al.* (2020) did this once for each particle, here 20 minimizations were calculated and the lowest energy state was selected to indicate the initial domain state. Each particle's initial domain state of Single Domain (SD), Sin-

gle Vortex (SV) and Multi Vortex (MV) was visualized using the open-source software ParaView (Ayachit 2015). Simulating the 20 upper hysteresis-loop branches was replicated for each particle using the same method as Nikolaisen *et al.* (2020). The applied field was swept from 350 mT and –350 mT in 5 mT steps. Hysteresis loops and backfield remanence curves were calculated for each 20 external field directions, chosen from a Fibonacci sphere (Mathematica code in the appendix) to achieve an approximately homogeneous distribution, presented in Fig. A1 and 'External field' column in Table A1. The numerical average of the hysteresis loops and backfield curves over the 20 field directions for each mesh geometry approximately represents a random spherical ensemble of equal particles. Values of M_{rs}, H_c and the calculated magnetic susceptibility at remanence (χ^*) were extracted from the average curves. (χ^*) is calculated by the first derivative of the hysteresis curve at 0 mT and does not directly correspond to conventional measurements of the magnetic initial susceptibility χ_0. The direction of magnetic remanence is a direct output from the micromagnetic modelling (in Cartesian coordinates) at each field increment
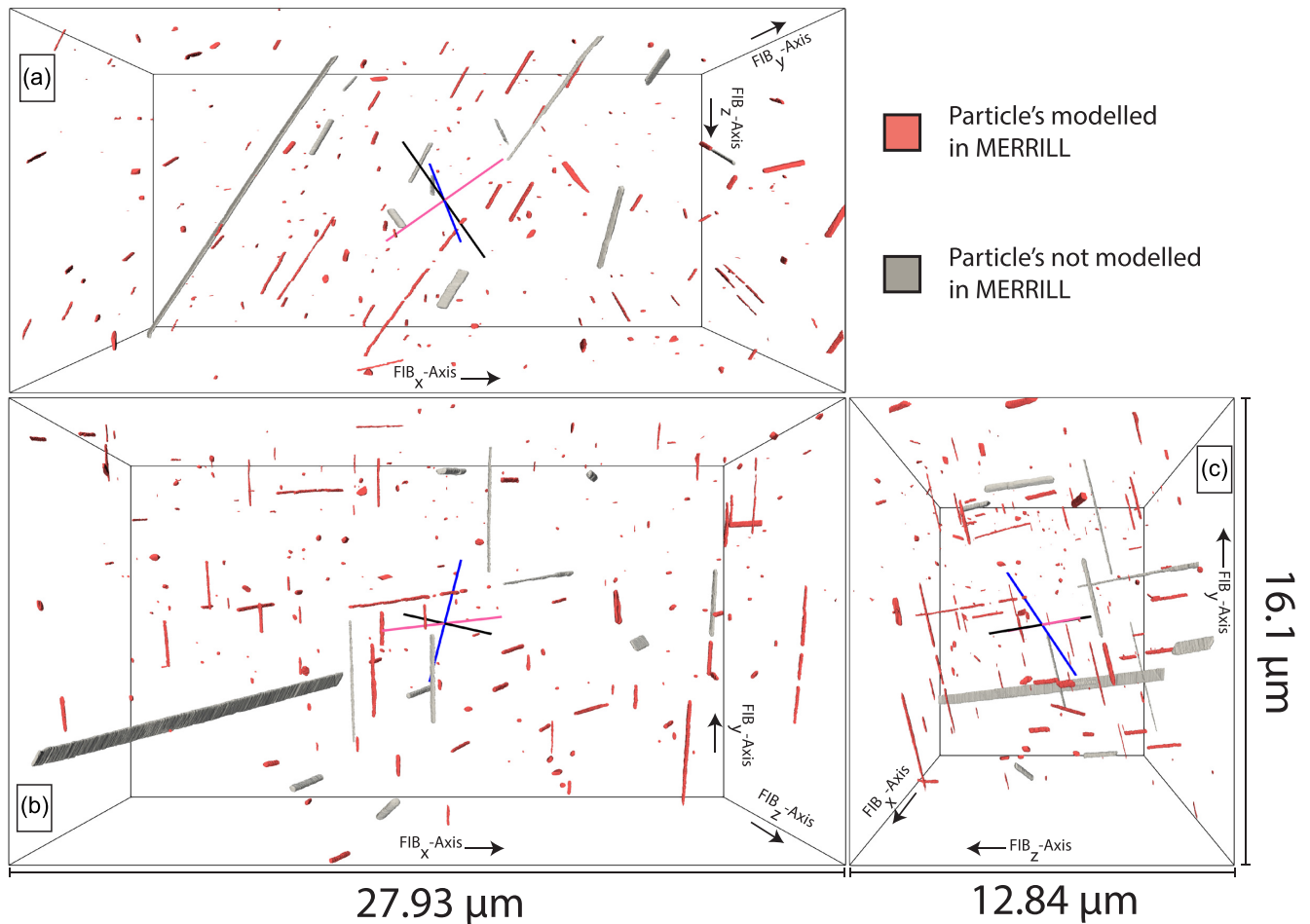
Figure 2. The three axis projections of the magnetite inclusions in the plagioclase with the dimensions 27.93 μm (FIB$_X$-axis), 16.1 μm (FIB$_Y$-axis) and 12.84 μm (FIB$_Z$-axis). (a) Projection down the FIB$_Y$-axis plane. (b) Projection down the FIB$_Z$-axis and c) projection down the FIB$_Y$-axis. The black arrows illustrate the positive axis directions of the modelled volume. Projection a is oriented to view down at the surface of the milled volume, presenting the same viewing direction as when studying a thin section. The coloured lines at the centre of the volume are the crystallographic axis direction of the silicate host, derived from EBSD that is discussed below. Black is [100]$_{plag}$, magenta is [010]$_{plag}$ and blue [001]$_{plag}$.

and presented in this publication as an average for all particles at 0 mT.

## 2.6 Experimental magnetic measurements

Plagioclase and orthopyroxene mineral separates were prepared by crushing bulk samples and isolating individual phases using a combination of magnetic separation and hand picking (Lundgaard *et al.* 2006), at the University of Aarhus. For measurement in the magnetometer, approximately 100 mg of the separates were placed in gelatine capules, representing 10–100 s of crystallites. Cyanoacrylate cement was used to immobilize the crystals of the plagioclase specimen and tightly pressed wadding for the orthopyroxene. Room-temperature hysteresis loops with maximum field 1 T were measured on a Princeton Measurement Corp. vibrating sample magnetometer at the Rock Magnetic Laboratory at NTNU and at the Institute for Rock Magnetism, University of Minnesota.

Hysteresis loops from a variety of coarse-grained magnetites were compiled to capture a range of multi-domain behaviours. A slice of natural, polycrystalline magnetite was measured in two orientations to observe the influence of sample shape anisotropy on the hysteresis loops, which are denominated MD2 nat1 and MD2

nat2 in this work. The specimen is dominantly magnetite in mm- to cm-scale grains with accessory serpentine and magnesite. Detailed chemical and magnetic characterization of this rock was reported by Pastore *et al.* (2019). In addition, two synthetic samples produced using different methods were also included. Wright Industries W6 is a synthetic, hydrothermally precipitated magnetite powder with a mean particle size of 12.1 μm (Krasa *et al.* 2003). MD1 poly is a polycrystalline sample produced by sintering Fe_2O_3 at 1300 °C in the reducing conditions given by Dieckmann (1982); full synthesis details in Church *et al.* (2011).

2.7 EBSD

The EBSD analysis was conducted on the Hitachi SU-6600 SEM at electron microscopy lab at IGP, NTNU, in low-vacuum mode using 20 kV accelerating voltage, an extraction voltage of 1.70 kV. The samples were mounted on metal pedestals at standard eucentric height with a tilt angle of 70 ° and working distance of 22.0 mm. To avoid geometric trapezoidal scan distortions in the maps, a beam scan voltage correction was implemented using a EM-Tec LAMC-15 large area magnification calibration standard (Sørensen *et al.* 2020). EBSD patterns were acquired using a NORDIF UF-1000
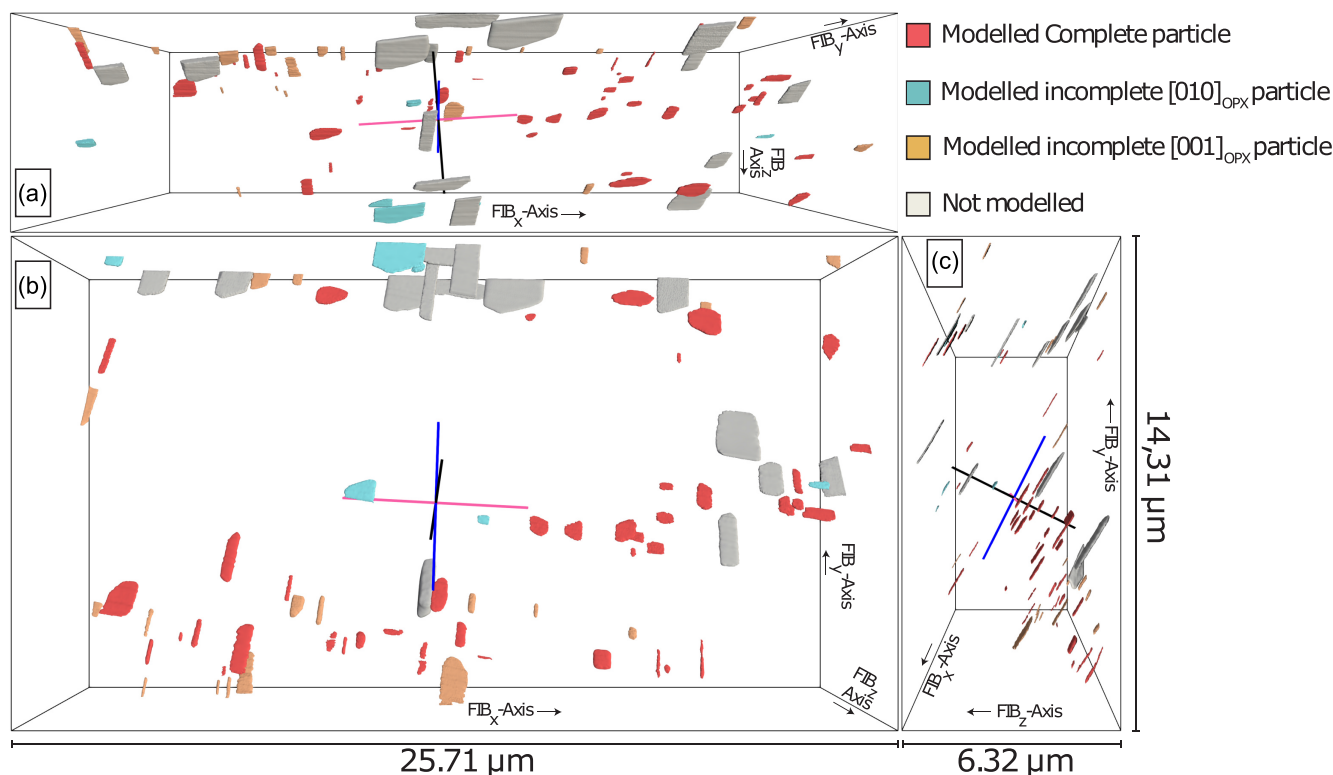
Figure 3. Three axis projection of the magnetite lamellea in orthopyroxene with the dimensions 25.71 μm (FIB$_X$-axis), 14.31 μm (FIB$_Y$-axis) and 6.32 μm (FIB$_Z$-axis). (a) Projection down the FIB$_Y$-axis, (b) projection down the FIB$_Z$-axis and (c) projection down the FIB$_X$-axis. The black arrows illustrate the positive axes directions of the modelled volume. Projection a is oriented to view down at the surface of the milled volume, presenting the same viewing direction as when studying a thin section. The coloured lines at the centre of the volume are the crystallographic axis direction of the silicate host, derived from EBSD that is discussed below. Black shows the $[100]_{opx}$, magenta the $[010]_{opx}$ and blue the $[001]_{opx}$ axis direction.

detector and the NORDIF 3.0 software. Indexing was done using the TSL-OIM 7.2 software at the Department of Material Science and Engineering, NTNU. EBSD data cleanup was done according to the procedures described in Sørensen *et al.* (2020), checking the consistency of indexing and cleanup procedures. EBSD plotting was done using MTEX (Bachmann *et al.* 2010), version 5.7. The regions of the EBSD analysis are indicated by the black dotted boxes in Figs 1 b and 1c. The crystallographic directions of the silicate crystal are directly extrapolated to the milled volume by projecting the projecting all results parallel to *FIB$_Y$* axis, then aligning *EBSD$_X$* with *FIB$_X$* and *EBSD$_Y$* with *FIB$_Z$*.

The crystallographic relationship between magnetite needles and the plagioclase host are identified in *An$_{50}$* by Sobolev (1990) and *An$_{60-70}$* by Ageeva *et al.* (2020). Exsolved magnetite in those studies was documented to crystallize in several orientations: one parallel to $[001]_{plag}$, two others in a plane perpendicular to $[001]_{plag}$ on the opposite sides of the $(010)_{plag}$ plane, almost coinciding with $(150)_{plag}$ and $(1\bar{5}0)_{plag}$ planes (Sobolev 1990), and two more orientations subparallel to $(112)_{plag}$ and $(\bar{3}12)_{plag}$ planes (Ageeva *et al.* 2020). For pyroxenes, ilmenite exsolution lamellae are present as coherent rods and blades where $(001)_{ilm}$ is epitaxially intergrown on $(100)_{px}$, and the *a*-axis of ilmenite is parallel to the *c*-axis of pyroxene (McEnroe *et al.* 2004). Specifically magnetite is studied in detail by Fleet *et al.* (1980) and reported to only exsolve as 'Z' inclusions oriented parallel to the $[001]_{px}$ axis, lying in the $(100)_{opx}$ plane (Champness & Lorimer 1974; Kirby & Etheridge 1981; Reiche & Bautsch 1985).

It is important to emphasize that the dataset and sample were not primarily set up for these analyses. The EBSD analysis is taken of

the thin section surface within both the plagioclase and orthopyroxene crystal's in close vicinity, but not directly on the milled sections, because of the ion beam contamination (platinum and gallium) and destruction of the milling area. To achieve better alignment we recommend that the EBSD is measured before performing the FIB-nt. From the angled carbon rods added to the platinum cover, we can observe when stacking the slices that the amount of removed material during milling is not constant. By varying slice thickness we estimate a degree of misalignment at $\approx$5° to a particle's phi and theta angle. Further development in interpolation techniques would improve the accuracy when integrating EBSD analysis. Because of the uncertainties explained above, we only used known magnetite orientations in silicates from highly detailed studies. Then, interpreting the population directions of magnetite in our FIB volumes, to the closest crystallographic direction know have exsolved iron oxides.

3 RESULTS

3.1 Plagioclase

This milled volume of plagioclase contain a total of 246 particles of magnetite and we were able to run hysteresis loops for 234 of these (red coloured particles in Fig. 2). In this volume of plagioclase the magnetite forms three different patterns differentiated by shape and size. The crystallographic orientations are all interpreted from EBSD data and discussed below. The first and most notable are magnetite 'plates' or 'blades' that are a few to several micrometers long,

800 nm wide and 200 nm thick (grey in Fig. 2). The elongation axis for these magnetite blades are oriented normal to the $(150)_{plag}$ plane and subparallel to the $(\bar{3}12)_{plag}$ plane. Because of their size these particles were not modelled in MERRILL. Furthermore, based on their morphology, we cannot definitely confirm that they are indeed magnetite. As they occur in the lower section of the milled volume, the BSE signal and the focus is weaker for the bottom third. The second set of particles are magnetite rods/needles with the major axis measuring up to several microns. These rods are very thin and appear subparallel to the $[001]_{plag}$ direction. The third set are smaller (sub 0.2 μm) prismatic magnetite particles with their elongation normal to the $(1\bar{5}0)_{plag}$ direction and subparallel to $(112)_{plag}$ plane. These inclusions are often associated with coexisting zircon and are in contact with an accessory mineral that has a lower BSE contrast than the plagioclase host (possibly quartz). While these three crystallographic orientations are the most populated there are 3–4 other orientations that can be observed by a few particles. Fig. A5 provides a comparison between optically visible exsolutions and EBSD measurements of the area right above the milled site. Two of these additional directions are subparallel to the $(1\bar{5}0)_{plag}$ (red line in Fig. A5) and $(150)_{plag}$ (orange line in Fig. A5) planes. The particles in these other directions are modelled in MERRILL and added to the final results. However they will not be given any further consideration within this paper as their populations are too low to make a significant contribution to the total remanent magnetization.

3.2 Orthopyroxene

This milled volume of orthopyroxene contains 82 magnetite particles of which hysteresis loops were calculated for 68. The majority of these particles are oblate ($a > b \gg c$) This sample contains discrete grains of ortho- and clinopyroxene, with orthopyroxene as the most dominant pyroxene. inverted pigeonite (in-pig) exists as lamellae and smaller exsolved grains within orthopyroxene. Magnetite is commonly observed as larger oxy-exolution lamellae, but also irregularly as exsolution lamellae in orthopyroxene. They are always in contact with thin (<200 nm) in-pig lamellae and elongated in the $[001]_{opx}$ direction and flattened parallel to the $(100)_{opx}$ plane. The determined crystallographic orientations from our EBSD analysis, identified exsolved oxide and inverted pigeonite lamellae in the $(100)_{opx}$ plane. From Fig. 3 it can be seen that 24 particles (coloured teal and yellow) are truncated by the milling volume, and that these truncated particles contribute to the population of $[010]_{opx}$ oriented particles. Although these truncated particles were simulated, their contribution to the total moment are less compared to the 44 complete particles (red in Fig. 3).

3.3 Micromagnetic properties

For the plagioclase volume, the 234 modelled particles can be divided into 168 single-domain (SD), 60 single vortex (SV) and 6 multi-vortex (MV). Within the orthopyroxene volume there are 24 SD, 27 SV and 17 MV, based on the lowest of 20 energy states minimized from a random seed. A selection of modelled particles from the orthopyroxene is visualized in Fig. 4 with magnetic parameters in Table 2 for three different remanent states: column (1) the domain state representing the lowest of 20 energy states minimized from a random seed, column (2) the saturation remanent state obtained after applying a saturating field in the direction (Fig. A1) that yielded the max H_c and column (3) the saturation remanent state obtained after applying a saturating field in the direction that yielded

the max M_{rs}/M_s. OPX026 is an SD particle where the maximum H_c is when fields are at a 40° angle to the particle elongation axis. The maximum M_{rs}/M_s is found for external fields applied at a low angle ($\leq 20°$) to the elongation axis. For SV and MV particles OPX058, 036 and 071, the field direction yielding max H_c is aligned with the shortest axis and the field direction yielding max M_{rs}/M_s is in the direction of the elongation axis.

Fig. 5 and Table A1 compare the hysteresis curves and micromagnetic properties for both orthopyroxene (a) and plagioclase (b), where each hysteresis curve represents the sum of loops for all particles for a given field direction. Two hysteresis curves representing extracted single silicate crystals of orthopyroxene and plagioclase, measured on a vibrating sample magnetometer (VSM) are shown in blue for orthopyroxene (Fig. 6a) and plagioclase (Fig. 6b). The red curves in Fig. 6 are the result of summing all calculated hysteresis loops over all the external field directions, weighted by M_s, for orthopyroxene (a) and plagioclase (b). Using the hysteresis loops of pure MD magnetite in Fig. 7 as a reference, an estimate of the proportions of MD vs SD-MV particles in the orthopyroxene separates can be made using a non-negative least-squares approach (Lawson & Hanson 1995) which combines different weight contributions of the MERRILL and MD curves to obtain a best fit calculation that resulted in a hysteresis curve (Fig. 7b) composed of 48 per cent W6 spec 7, 29.4 per cent MD2 nat1, 16.7 per cent MD2 nat2 and 5.6 per cent MERRILL (Table 4). The total error between the optimized and measured single crystal hysteresis loops shows an average deviation between the two curves of 1.64 per cent (red curve in Fig. 7b). The MD curves in Fig. 7(a) have a variable rate in approach to saturation. As the gradient ($1/N$, Stacey & Banerjee 1974) of the hysteresis slope is dependent on the internal demagnetization factor (N), the difference in approach to saturation between the MERRILL and single crystal curve is the higher demagnetization factor of the larger MD magnetite. Calculating the fraction of remanence contributed by each of the MD and SD-MV fractions yields 41.7 per cent W6 spec 7, 17.2 per cent MD2 nat1, 12.6 per cent MD2 nat2 and 28.4 per cent MERRILL (Table 4).

The highest calculated MERRILL hysteresis parameters in the orthopyroxene, M_{rs}/M_s values of 0.68–0.72 in Table A1 agree well with the magnetite elongation directions, which are subparallel to $[001]_{opx}$ (Fig. 3c). They correspond to field directions 6, 11 and 14 (Fig. A1).The lowest M_{rs}/M_s values of 0.132–0.153 are observed for field directions normal to the flattened blade surfaces of the magnetite lamellae and subparallel to $[100]_{opx}$ at the field directions 13, 15 and 18. H_c values show a different trend: intermediate values of $\approx$17 mT are observed parallel to the elongation direction of magnetite, maximum values of 27–32 mT are observed normal to the flattened blade surfaces, and minimum values of 9–10 mT are observed along the intermediate length axis. For χ^* the maximum of 17 (SI) is approximately parallel to the $[010]_{opx}$ in external field direction 8. The minimum χ^* with 2.7 (SI) is sub parallel to $[100]_{opx}$ in field directions 15 and 18, which are the same directions as the lowest M_{rs}/M_s.

In the plagioclase, the highest M_{rs}/M_s values of 0.510–0.518 in Table A2 aligns with the fitted $[\bar{1}\bar{2}8]_{plag}$ direction and in the external field direction 12 and 15. Which is highly influenced by the primary $[001]_{plag}$ cluster of oriented magnetite, but offset by the contribution of the lesser magnetite populated normal to the $(150)_{plag}$ plane. The lowest M_{rs}/M_s at 0.198 oriented at $\phi = 75°$ to the maximum M_{rs}/M_s in the external field direction 8. The maximum H_c of 46 mT is in direction 11 and the minimum of 22 mT in direction 13. For χ^* the maximum of 5.8 (SI) is in the external field direction 9 and the minimum of 3.3 (SI) in the external field direction 16. These results
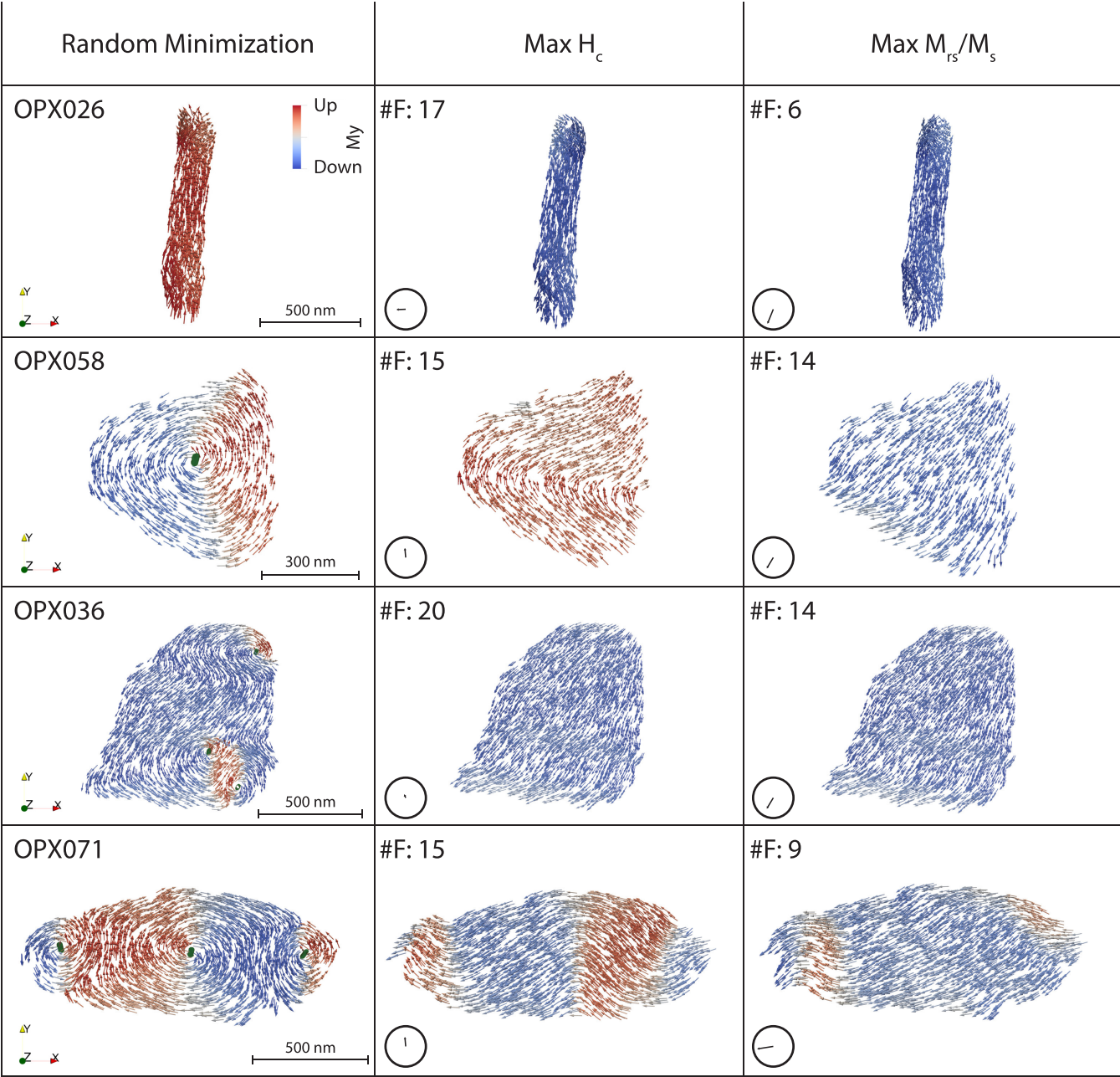
Figure 4. Micromagnetic models of selected particles from the orthopyroxene. The random minimization states (left-hand column) are the remanent domain states having the lowest of 20 energy minimizations from a random seed. The maximum H_c (central column) and maximum M_{rs}/M_s (right-hand column) states are saturation remanent states calculated from the hysteresis loops for individual external field directions (#F) that yielded the maximum coercivity and saturation remanence, respectively (Fig. A1). The FIB$_X$ and FIB$_Y$ direction of #F is visually represented as a stereographic projection of the upper hemisphere, for each particle by the arrow at the bottom left corner. All external fields have a positive FIB$_Z$ direction oriented out of the page. An accompanied figure for particles in the plagioclase can be found in Fig. A7.

Table 2. Hysteresis parameters for the magnetic models in Fig. 4. The average H_c (mT) and M_{rs}/M_s is representative for the specific particle over all 20 external fields. The two last columns represent the direction of the field that resulted in the maximum H_c (mT) and M_{rs}/M_s. Field direction numbers refer to Table A1 where the corresponding coordinates are listed in columns 'External field'.

Particle	Domain state	Average H_c (mT)	Average M_{rs}/M_s	Field direction (Nr)	H_c (mT)	Field direction (Nr)	M_{rs}/M_s
OPX026	SD	31.7	0.46	17	57	6	0.89
OPX058	SV	13.5	0.52	15	39	14	0.94
OPX036	MV	14.2	0.58	20	52	14	0.945
OPX071	MV	15.4	0.50	15	35	9	0.94
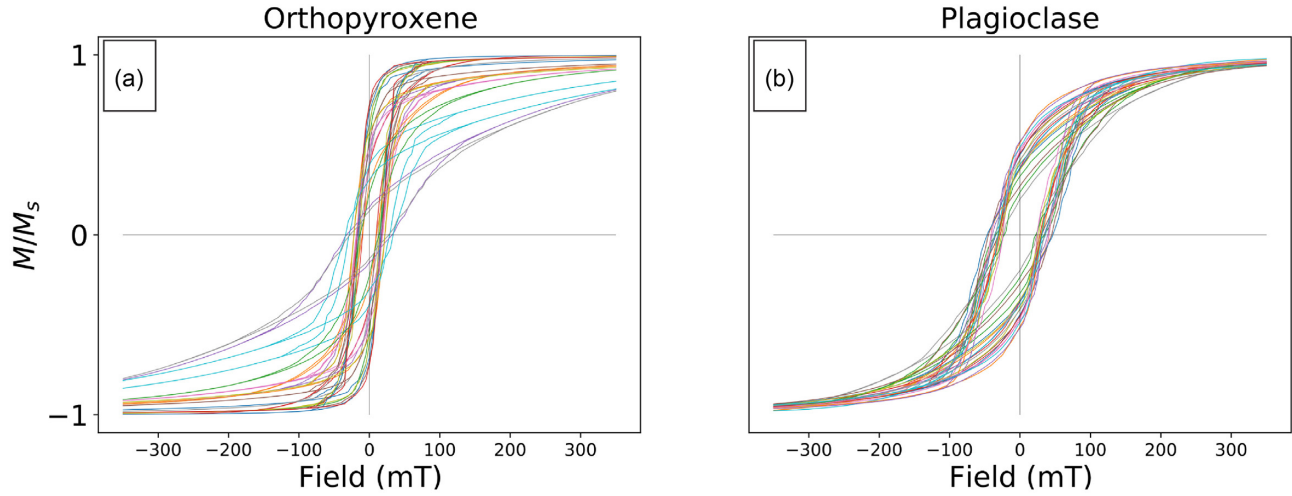
Figure 5. Magnetic hysteresis curves for all particles orthopyroxene (a) and in plagioclase (b) for the individual fields direction from -350 to 350 mT. Each loop is generated by summarizing all particle's hysteresis for a different applied field. The resulting H_c and M_{rs}/M_s for each loop is presented in Table A1.
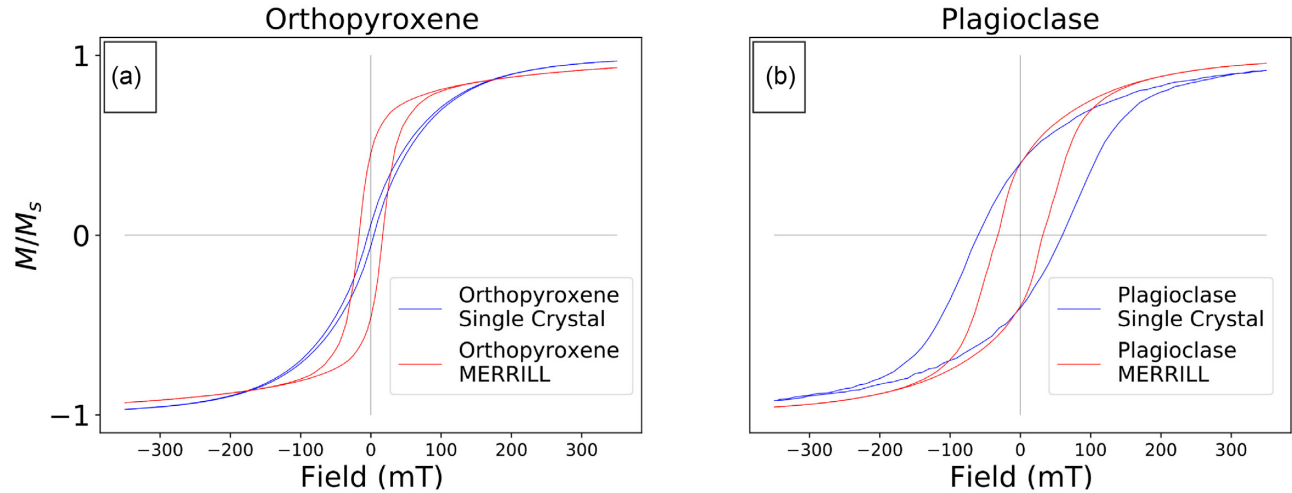
Figure 6. Magnetic hysteresis curves for fields from -350 to 350 mT of a single silicate crystal (blue) and MERRILL calculations (red) of (a) orthopyroxene and (b) plagioclase from B16 sample. H_c and M_{rs}/M_s is presented in Table 3.

indicate that for plagioclase the lowest M_{rs}/M_s and χ^* are in the same direction as maximum H_c.

Table 3 summarizes the micromagnetic properties for the hysteresis curves and the extracted silicate volumes providing an estimate for the magnetic properties as they are measured on the bulk sample. The first and third row represents the measured single-crystal hysteresis and second and fourth row the milled volumes. Volume (V) is calculated from the weight of the silicate crystal with an average mineral density and the MERRILL volume is estimated by the size of the FIB cube (Figs 2 and 3). The saturated moment (μ_s), M_{rs}/M_s and H_c are interpreted from the hysteresis. Saturation magnetization (M_s) is calculated μ_s/V and represents the magnetic intensity of the magnetite inclusions.

4 DISCUSSION

4.1 Orthopyroxene hysteresis

A comparison of the measured hysteresis loop of the orthopyroxene single crystals with the MERRILL calculated hysteresis loop in Fig. 6 highlights the limitations of this approach. Based on optical

observations, the most abundant magnetite occurs in two groups of 500–300 μm and 50–100 μm oxy-exsolved inclusions of MD magnetite and ilmenite. The area targeted for MERRILL calculations, on the other hand, focused on the rarer occurrence of much smaller magnetite lamellae (Figs A2c and A4). Of the 68 particles within the milled orthopyroxene volume (Fig. 3), the largest particles that were completed in MERRILL have a volume equivalent to a sphere diameter (EVSD) of <400 nm and adopt MV states. The median H_c and M_{rs}/M_s values of these particles are 0.02 T and 0.51, respectively—leading to considerably higher coercivity and remanence in the calculated loop compared to the measured one. The best hysteresis curve fit in Fig. 6(b) implies that ≈ 94 per cent of the magnetic signal is due to MD magnetite (Figs 6b and Table 4. The OPX M_s values in Table 3 provide the estimate that OPX MERRILL represents $177/2234 \approx 8$ per cent of the bulk OPX single-crystal measurement. Together, this defines a calculated range of the MD contribution to the measured single-crystal hysteresis for this particular sample between 92 and 94 per cent. Even though the MERRILL curve contributes only 6 per cent to the total saturation magnetization of the sample, its SD-MV particles carry a disproportionately large 28 per cent of the remanence in these silicates (Table 4).
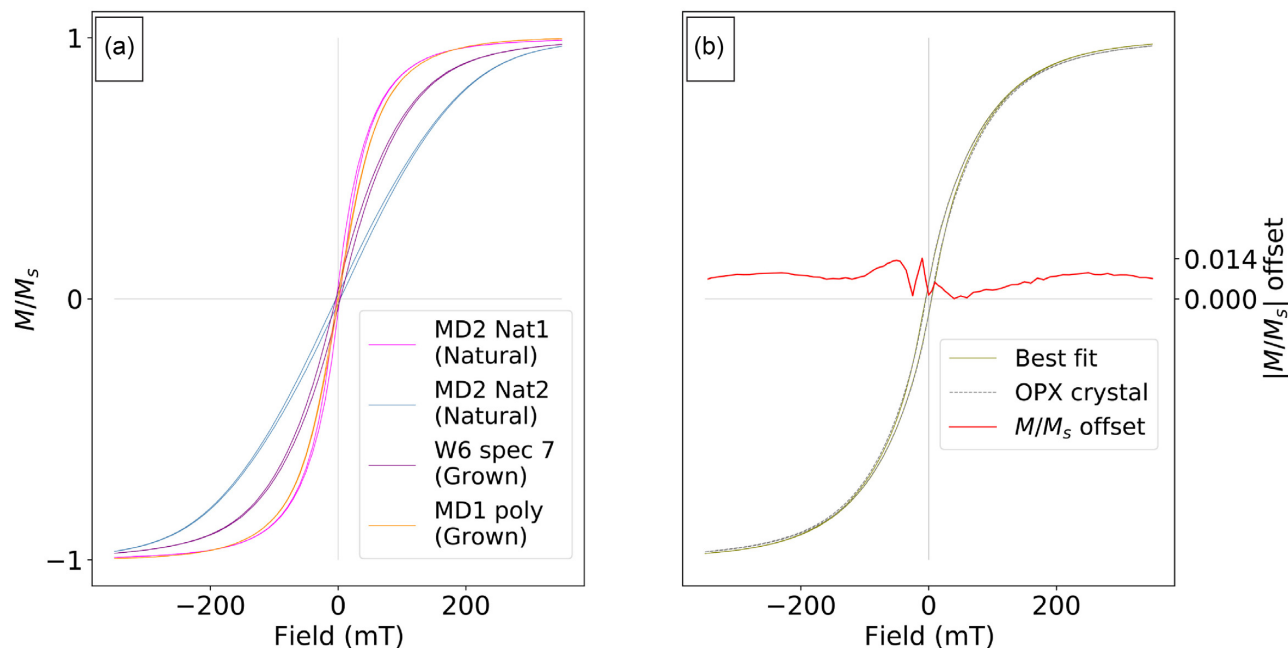
Figure 7. (a) Magnetic hysteresis curves for fields from -350 to 350 mT of natural and grown magnetite with multi domain magnetic parameters that have no influence of single domain material. (b) The resulting composite curve by non-negative least-square optimization compared to the measured single crystal of orthopyroxene. H_c and M_{rs}/M_s is presented in Table 4.

Table 3. Magnetic properties for the plagioclase and orthopyroxene single crystal measurements and the milled volumes calculated with MERRILL. For the crystals, the saturation magnetization M_s is calculated by dividing the crystal saturation moment (μ_s) by the crystal volume V. The susceptibility χ^* is the slope of the upper hysteresis branch at zero field.

Sample	V (μm^3)	M_{rs}/M_s	μ_s (μAm^2)	H_c (mT)	M_s (A m^{-1})	χ^* (SI)
PLAG single crystal	4.26×10^{-2}	0.40	2.2	65.04	51.6	2.95
PLAG MERRILL	5.8×10^{-9}	0.39	5.44×10^{-7}	36.97	93.8	4.3
OPX single crystal	2.45×10^{-2}	0.06	54.7	9.26	2234	7.6
OPX MERRILL	2.33×10^{-9}	0.46	4.1×10^{-7}	21.9	177	10.9

Optical and electron microscopy observations indicate that thin magnetite lamellae which correspond to the model volume in Fig. 3 are scarcer than 6 per cent and occur in patches with associated In-Pig lamellae (Figs A3 and A4). However, there are also grain boundary and crack-filling Fe-oxides (Figs A2a, A2b, A2e and A3). These particles are not identified properly, but would contribute to the measured hysteresis and could therefore explain the minor differences between the optical estimate (<6 per cent) and that based on the magnetic properties (6–8 per cent). An overall bulk estimate of magnetite based on optical microscopy observations puts the MD fraction at 97–98 per cent.

4.2 Plagioclase hysteresis

For plagioclase in Table 3 the M_s for measured hysteresis is 51.6 (A m^{-1}) compared with 93.8 (A m^{-1}) for the MERRILL calculations. This nearly twofold greater magnetization of the milled volume can be explained by selective sampling. Since the limitation for the milling volume is about 25 μm $\times$ 25 μm $\times$ 15 μm (L$\times$W$\times$H) it is important to select an area with a high concentration of visible inclusions. It is, therefore, highly probable that the area selection is biased towards a higher concentration of larger particles, since it is difficult to observe and evaluate the concentration of smaller inclusions that are suitable for modelling in MERRILL.

The much higher H_c of the measured hysteresis loop (Fig. 6b) is consistent with the idea that, on average, particles contained in the feldspar crystals are smaller (more SD) than those represented in the region selected for FIB milling. The modelled particles with H_c in the range of 65 mT are predominantly SD particles with M_{rs}/M_s ≈ 0.5. The particles with M_{rs}/M_s in the range of 0.4 are primarily SV to MV particles with 5 mT $<H_c<$ 40 mT. The difference in H_c values of 37 mT (model) and 65 mT can also be due to the effect of dislocations, surface stresses and pinning sites. These natural imperfections delay the magnetization change and increase H_c, and are not included in the micromagnetic model, where by the latter underestimates H_c.

These observations demonstrate the importance of recognizing the sampling bias that is inherent with a highly targeted approach such as FIB micromagnetic nanotomography, which self-selects particles in the SD-MV size range (limited at small sizes by the finite thickness of the slices and at large sizes by the computational constraints of the micromagnetic simulations). The fact that observations are destructive, and contained within a limited field-of-view that may poorly represent the particle size distribution in the whole crystal, must also be considered. Techniques such as high-resolution X-ray tomography, which are capable of non-destructive imaging of entire single crystals (Suuronen & Sayab 2018) have the potential to reduce sampling bias associated with the limited

Table 4. Magnetic properties M_{rs}/M_s and H_c (mT) for the MD hysteresis curves and the MERRILL calculated hysteresis curve. Weight percent (wt. per cent) and the remanence fraction [RF (per cent)] is the contribution of each hysteresis curve to the calculated best-fitting curve.

Hysteresis	Mass (g)	M_{rs}/M_s	Hc (mT)	wt. per cent	RF (per cent)
MD1 poly	5.7×10^{-4}	0.01	0.723	0	0
MD2 nat1	1.7×10^{-1}	0.05	2.5	29.4	17.2
MD2 nat2	1.7×10^{-1}	0.017	3.135	16.7	12.6
W6 spec 7	4.9×10^{-3}	0.033	3.35	48.3	41.7
MERRILL	7.23×10^{-10}	0.46	21.88	5.6	28.4

field of view. However, such methods are currently only able to detect particles in the SV range and above due to a combination of contrast and spatial resolution limitations. A multiscale, correlative approach, that combines high-resolution X-ray tomography of the whole crystal with targeted FIB nanotomography and transmission electron microscopy, would enable full characterization across the entire range SP-SD-SV-MV-MD domain states. Pushing micromagnetic simulations into the MD range, however, remains a significant computational challenge.

4.3 Magnetic anisotropy of M_{rs}/M_s, H_c susceptibility and the deflection of remanent magnetization

The following subsections discuss and analyse the modelled average anisotropy over all particles for three parameters based on the 20 modelled field directions. These parameters are not completely independent, but focus on different aspects of the magnetic ensemble. M_{rs}/M_s indicates the strength of remanence, H_c the stability of remanence and χ^* the overall ease of field response of the magnetization structures. Because these are average results for individual field directions, the values for individual particles can vary significantly. As the different sections of the discussion do cross reference and depend on each other, we have compiled the following Figs 8, 9 and 10into the single supplementary Fig. A6.

4.3.1 *Anisotropy of M_{rs}/M_s and H_c*

The field orientation dependence of ensemble hysteresis properties is illustrated in Fig. 8 using the colour and size of the symbols to indicate M_{rs}/M_s and H_c from Table A1, respectively. The crystallographic orientations of the pyroxene and feldspar single crystals, as determined by EBSD are indicated, along with reference crystallographic directions and planes. Contours illustrate the distribution of elongation axes of the magnetite particles, as determined by FIB. In the orthopyroxene (Fig. 8a) the primary cluster of elongation axes is oriented along $[001]_{opx}$ and a smaller cluster elongated along $[010]_{opx}$. Whilst the maximum M_{rs}/M_s trend corresponds well to that expected based on shape anisotropy, the H_c trend is arguably less intuitive, with highest H_c in the direction of the lowest M_{rs}/M_s. Because the particle distribution is dominated by SD and SV domain states, the M_{rs}/M_s and H_c anisotropy should be different from the anisotropy expected for Stoner–Wohlfarth SD hysteresis. The shape of the modelled OPX MERRILL hysteresis loop (Fig. 6a) would usually be classified as SD dominated even though it is not. Because the calculated magnetic anisotropy is different from the Stoner–Wohlfarth model, it is likely dominated by the non-SD states in the modelled particle ensemble.

Magnetic models in Fig. 4 represent typical particles that adopt SD, SV or MV remanent states after energy minimization from a

random seed, but display different remanent states after exposure to a saturating field. For example, crystal OPX026 is an approximately 1-μm-long needle that adopts an SD state after random minimization (left-hand image in Fig. 4) and after exposure to a saturating field applied close to its elongation direction (right and central image in Fig. 4). The other crystals in Fig. 4 adopt SV or MV states after random minimization, but a range of more SD-like buckling states (e.g. Aharoni 2000) after exposure to saturating fields in different directions. Fig. 4 demonstrates that the maximum M_{rs}/M_s occurs for fields applied along the long axis, and the minimum M_{rs}/M_s for fields along the short axis. When the external field is oriented at a high angle to the elongation axis, the switching takes place by a different succession of magnetization structures. An SD flower state at 0 mT rapidly nucleates an oscillatory buckling configuration with a shorter wavelength. This state is now relatively stable while the magnetization slowly rotates towards the external field direction. At higher opposite field strength the oscillatory buckling state nucleates a vortex. In the case of OPX071, the maximum coercivity H_c is observed for fields applied at a high angle to the elongation direction, where the adopted oscillatory buckling state in Fig. 4 (OPX071,#F:15) can be reversibly changed between 0 and 35 mT. At higher absolute fields the magnetization structure switches irreversibly and finally nucleates a single vortex. With external fields oriented subparallel to the particle's elongation axis the domain structure at zero field is reminiscent of a SD flower state. Increasing the field in opposite direction generates oscillatory buckling states DeSimone *et al.* (2005) with long wavelengths which eventually nucleate to a single vortex. Further field increase propagates the vortex core towards the particle edge and after de-nucleation transforms to a field-aligned flower or SD state.

In the plagioclase (Fig. 8b) the anisotropy of hysteresis parameters is weaker than in pyroxene. Contours indicate three distinct populations of particles with the most populated in the $[001]_{plag}$ orientation and the lesser populated normal to the $(150)_{plag}$ plane and the normal to the $(1\bar{5}0)_{plag}$ plane. The highest M_{rs}/M_s values (yellows and greens in Fig. 8b) are observed in a plane defined by the primary and secondary clusters of magnetite elongation axes, where the lower M_{rs}/M_s is oriented in the direction of the pole for this plane. The absolute maximum M_{rs}/M_s aligns with the fitted $[\bar{1}\bar{2}8]_{plag}$ direction, which is highly influenced by the primary $[001]_{plag}$ cluster of oriented magnetite, but offset by the contribution of the lesser magnetite populated normal to the $(150)_{plag}$ plane. For H_c the highest values ($\geq$39 mT) occur where external field directions are oriented close to parallel with the $[001]_{plag}$ magnetite population. The lowest H_c is quite distinct and occurs where the external field is at the highest angles to the main magnetite population and their elongation directions. In contrast to the orthopyroxene, the direction of maximum M_{rs}/M_s and H_c is close to the elongation direction of magnetite. A correlation that is theoretically expected, based on the Stoner–Wohlfarth model of SD hysteresis.

4.3.2 *Deflection of remanent magnetization*

The physical origin of the anisotropy of remanent magnetization are deflections of the individual grains towards collective preferred directions. In Fig. 9 this effect is visualized by showing the averages of the deflected remanence directions (red marks) for all modelled field directions. The direction of the remanence vectors for magnetic particles in orthopyroxene (Fig. 9a) are consistent with the field directions with the highest M_{rs}/M_s in Fig. 8(a), highlighting the strong ferrimagnetic fabric in OPX aligned with the magnetite
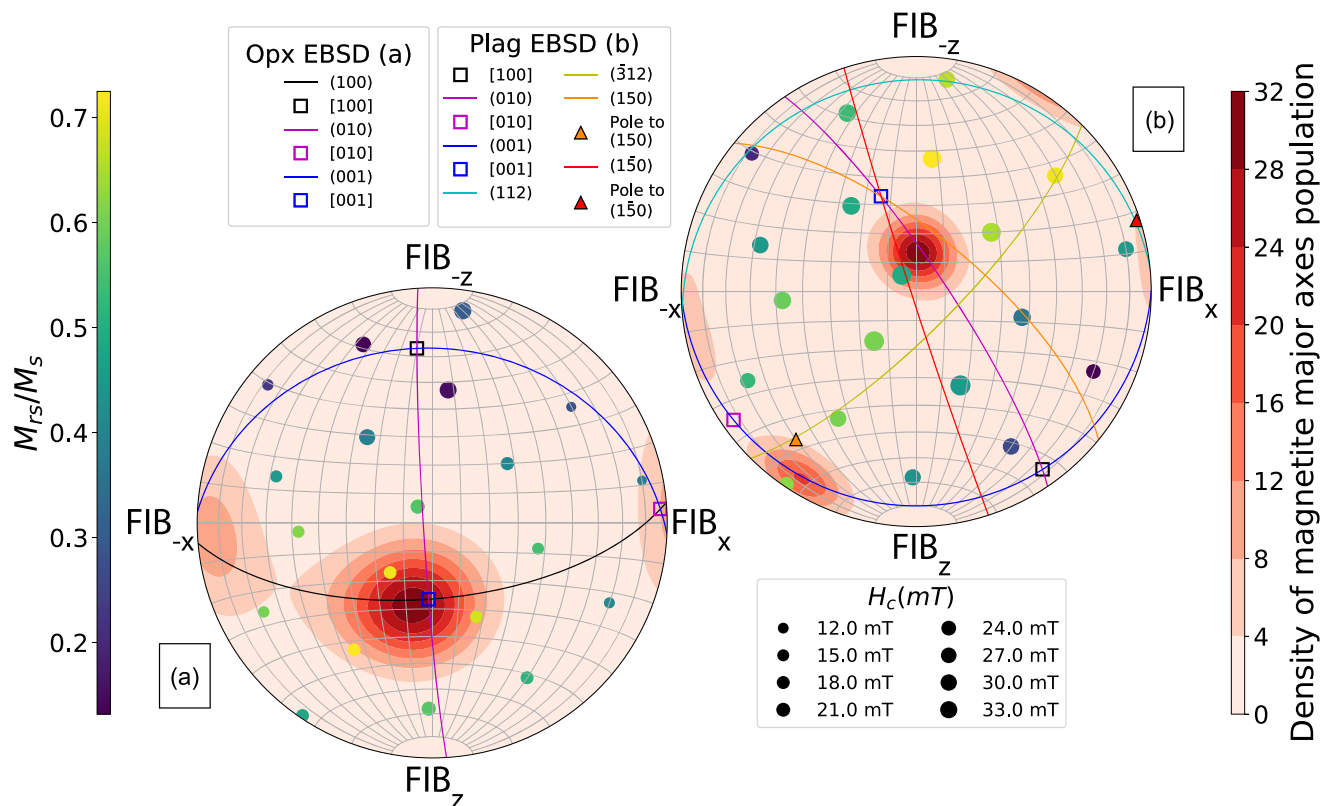
Figure 8. Stereographic projection normal to the FIB_Y-axis for both orthopyroxene (Fig. 3a) and plagioclase (Fig. 2b). Red contours show the population of the elongation axis for the particles and the round markers the external field direction. Round marker size is the total coercivity and colour is the strength of the remanence. Lines show the crystallographic planes of the silicate host and the square markers the crystallographic direction.

elongation axis. Two of the 20 remanence vectors in Fig. 9(a) form a group outside the main clusters. They belong to the external field directions 2 and 7 (Table A1 and Fig. A1), and are oriented in the $[010]_{opx}$ direction. The group is separate, because it is populated by a relatively large fraction of particles with elongation axes along the $[010]_{opx}$ (Fig. 8a), like OPX071 in Fig. 4. They can also lock a high remanent magnetization in this direction. For plagioclase, the directions in which the remanenance is deflected in Fig. 9(b) differ from the orientations of the M_{rs}/M_s and H_c in Fig. 8(b). The main direction of deflection of M_{rs}/M_s is in the $[010]_{plag}$ and almost perpendicular to the direction of maximal M_{rs}/M_s. Maximum H_c and M_{rs}/M_s are oriented in the $[001]_{plag}$ direction, but both also show an alignment with elevated intensities in the best-fitting plane for the remanence in Fig. 9(b). This behaviour is due to the fact, that in the best fit plane the exact direction of deflection or M_{rs}/M_s is relatively indetermined, because the two primary populations of elongation axes contribute in nearly equal amounts.

4.3.3 Anisotropy of magnetic susceptibility in the remanent state

The average absolute values of χ^* for both silicates lie in the range of 3–5 (SI), which coincides with Fig. 1 in Heider *et al.* (1996), where experimentally determined isotropic initial magnetic susceptibilities (χ_0) of magnetite fall in the range of 2–4 (SI). For pyroxene our χ^* reach values of 10–15 (SI) for field directions at low angle to the particles elongation axis indicating a substantial anisotropy. The ensemble magnetic susceptibility tensor ($\mathbf{k}$) for all pyroxene particles, where $\mathbf{k}_1 > \mathbf{k}_2 \gg \mathbf{k}_3$ describes an oblate anisotropy, where $\mathbf{k}_1$ is subparallel to the $[001]_{opx}$, $\mathbf{k}_2$ subparallel to the $[010]_{opx}$ direction

and $\mathbf{k}_3$ subparallel to the $[100]_{opx}$ direction (Fig. 10a). The $\mathbf{k}_1$ direction is correlated with the primary cluster of individual particle elongation axes, which is parallel to the maximum M_{rs}/M_s (Fig. 8a). The large ensemble value of $\mathbf{k}_2$ is related to the secondary peak of individual particle elongation directions in Fig. 8(a). The ensemble value of $\mathbf{k}_3$ is substantially smaller because no individual particle elongations are close to the corresponding direction of $[100]_{opx}$.

The micromagnetic models allow us to analyse which changes in the magnetization structure are responsible for the calculated susceptibilities. This is done by comparing the magnetization state $\mathbf{m}_1$ at 5 mT to the state $\mathbf{m}_2$ at -5 mT. If the lengths of the difference magnetization vectors $\Delta m = |\mathbf{m}_1 - \mathbf{m}_2|$ at all mesh nodes are similar, a global rotation of spins has occurred. If for some nodes Δm is much larger than for others, a localized shift of magnetization took place near the locations of higher Δm. For particle OPX071 with fields at a low angle to the elongation axis, inspecting the magnetization change shows that localized changes with high Δm occur via increased magnetization buckling. The same particle with a field at high angles displays much smaller global Δm, indicating a stiff magnetization structure which allows only tiny rotations in response to an external field.

The review by Biedermann (2018) investigates low field anisotropy of magnetic susceptibility (AMS) carried by silicates and shows that measuring the principal components of k in pyroxene single crystals can provide a wide range of results. Biedermann (2018) reviews the few studies that have conducted research on this subject and suggests that inconsistencies result from ferromagnetic inclusions or exsolved magnetic phases within the silicate. For these studies the AMS of exsolved phases can contribute to, or even dominate, the intrinsic paramagnetic magnetic anisotropy
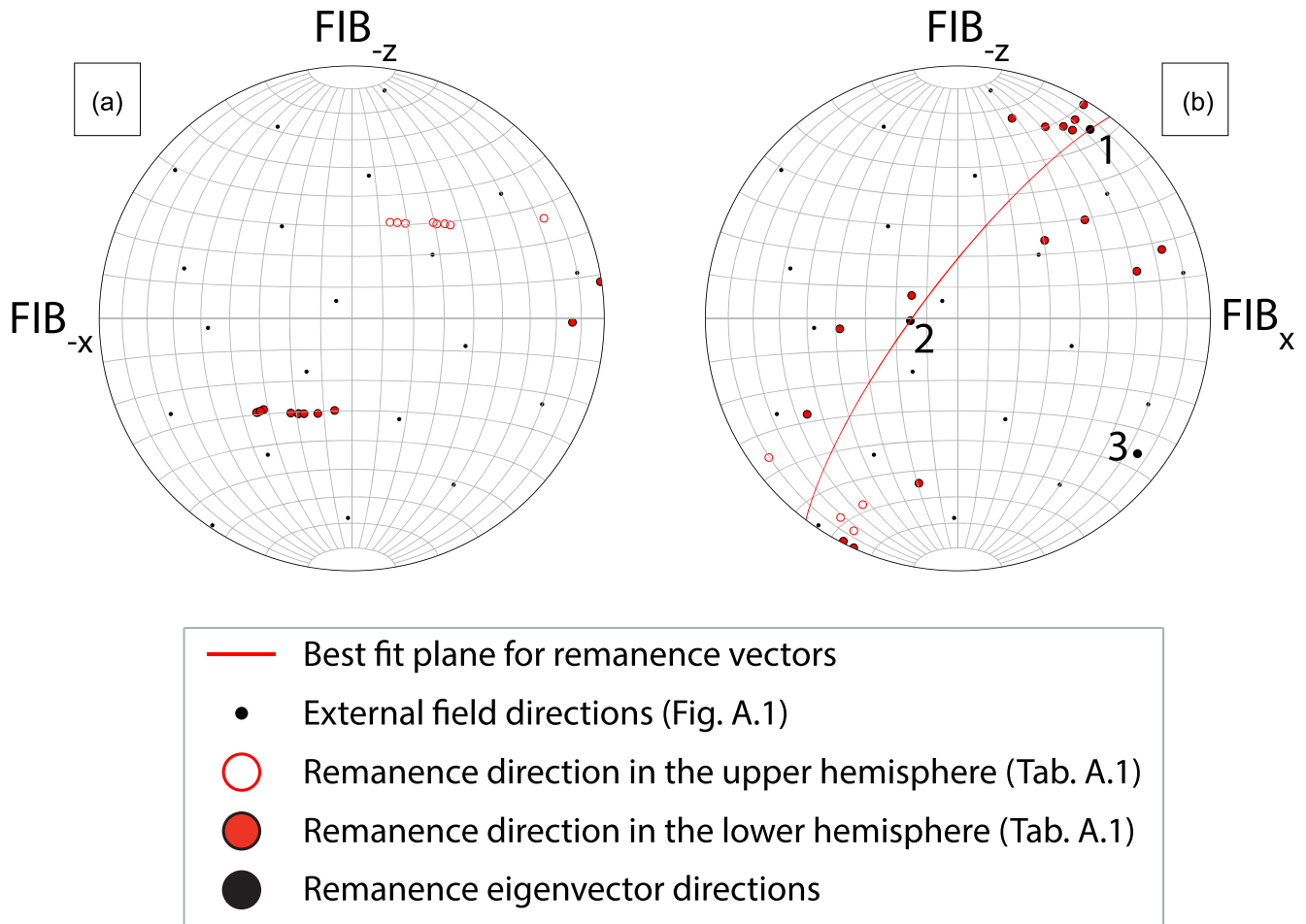
Figure 9. Deflected remanence vectors (red) for all modelled field directions (small black dots) after averaging over the particle ensemble. Red disks (circles) mark directions in the lower (upper) hemisphere (see Table A1). (a) Results for for orthopyroxene (OPX). (b) Results for plagioclase (PLAG). The red great circle represents the best fit plane for the deflected remanence vectors. Eigenvector directions of the remanent magnetizations are indicated by large numbered black disks. These deflections are the physical origin of the anisotropy of remanent magnetization.

of the silicate crystal itself. Methods to separate paramagnetic and ferromagnetic anisotropy are purely based on bulk measurements (Richter & van der Pluijm 1994; Martín-Hernández & Ferré 2007). Since our study removes the silicate host all together, there is no potential paramagnetic contribution, and our results can help to define the pure ferromagnetic contribution to the total AMS. Biedermann (2018) states that the degree of anisotropy increases with increasing amount of iron and the shape of the anisotropy changes from prolate to oblate, without providing any indication to where the additional Fe is situated. Their observation, combined with our results, where $k_1 > k_2 \gg k_3$, is consistent with the hypothesis that additional iron increases the ferromagnetic contribution to the AMS, by the formation of exsolved magnetite with an oblate anisotropy.

AMS in plagioclase single crystals is weak and often dominated by a diamagnetic component (Biedermann *et al.* 2020). Our results in Fig. 10(b) do reflect a lower ferromagnetic anisotropy than for pyroxene, with k_1 in the direction of $[010]_{plag}$, k_2 parallel to the particle elongation axis population slightly canted to the $[001]_{plag}$ direction (Fig. 8) and k_3 parallel to the $[100]_{plag}$ direction. The direction of the highest χ^* is oriented subparallel to the particle populations elongated normal to $(150)_{plag}$ and $(\bar{1}50)_{plag}$, rather than in the direction of maximum M_{rs}/M_s as seen for the orthopyroxene. A reason

is the way we calculated χ^* as the first derivative of the hysteresis curve at 0 mT. The calculated orthopyroxene curves (Fig. 5a) with the highest M_{rs}/M_s all have a steep gradient, but for the plagioclase curves (Fig. 5b) the gradients are all very similar. χ^* can be misleading because the magnetic models were minimized from a saturating field strength and the hysteresis resolution (field increments) is limited. However, the direction of maximum χ^* is supported by measurements of sunstone (andesine) single-crystal. Measurements by Hirt & Biedermann (2019) show k_1 in the direction of $[010]_{plag}$ and documented to be along the lath direction of ferrimangentic exsolutions. Other measurements that include labradorite concluded the high-field AMS to be very weak, but showing the k_1 in the $[010]_{plag}$ and k_3 in $[001]_{plag}$ directions (Biedermann *et al.* 2016; Hirt & Biedermann 2019).

Since we have chosen 5 mT steps for the external field there are details about the changes to the domain state at remanence that are not showing up in our simulations. Here further calculations with denser field steps and more field directions would be needed to provide a better understanding of these observations. The combination of FIB nanotomography and micromagnetic simulations in this case plays a valuable role in defining what our expectations should be for the intrinsic anisotropy of silicate-hosted magnetic inclusions.
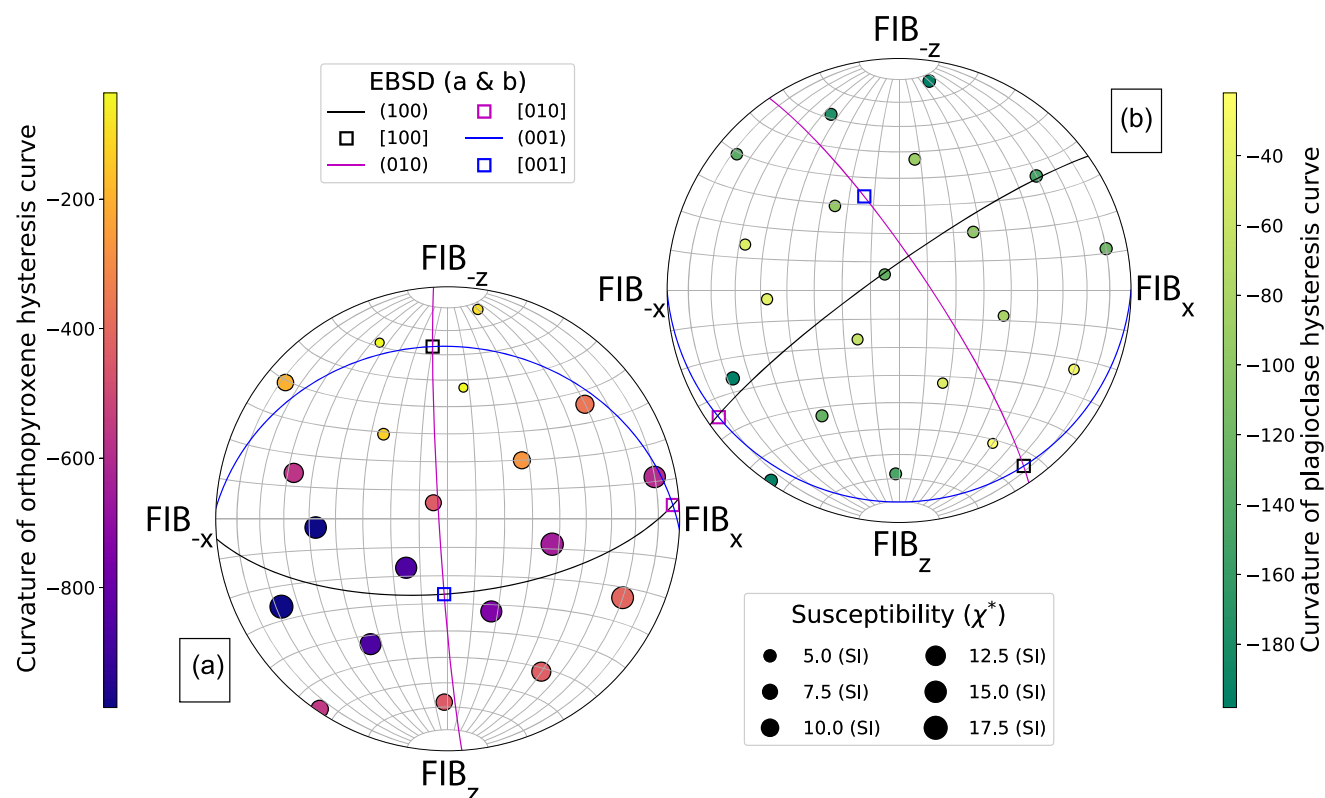
Figure 10. Stereographic projection down the y-axis for the milled volume in both (a) orthopyroxene (Fig. 3) and (b) plagioclase (Fig. 2). Round marker size is the calculated susceptibility (χ^*) in the direction of the external field. Colour is the curvature of the upper hysteresis branch at 0 mT in the direction of the external field.

4.4 Outlook

Micromagnetic modelling can provide valuable insights when interpreting bulk magnetic properties. Our comparison between single crystal measurements and the summarized MERRILL calculations highlight the magnetic diversity when analysing individual components at different scales. For plagioclase the measured and calculated hysteresis have a good overlap, but unexpectedly the measured hysteresis has a higher coercivity that our model was not able to replicate. One of reasons may be a selection bias of the FIB volume, but also unmodelled influences on coercivity are possible. Our results show that for plagioclase there is only a slight difference in the magnetic properties when analysing substantially different volumes. For the pyroxene our study highlights exactly how complicated the analysis of such silicates can become. This complexity is demonstrated by the disagreement between the measured and calculated hysteresis loops, that separately indicate there will be a deviation in the magentic properties when analysing different volumes. From our calculations the directions of remanence, susceptibility, high H_c and high M_{rs}/M_s are strongly oriented in specific crystallographic orientations. These important results, even at the scale of single-crystal measurements can be masked by secondary magnetic particles, magnetic inclusions and magnetic exsolutions in coexisting silicates, like quartz inclusions in plagioclase and inverted pigionite in the orthopyroxene. These are challenges that rock magnetism has to overcome and the results from Nikolaisen *et al.* (2020) and this study, provide a pathway to tackle this monumental task. Our models/calculations identify the primary oxide carriers of stable remanence, their geometries and how these are situated within the host and most importantly their micromagentic

properties, thereby illustrating the importance of further studies that combine FIB nanotomography and micromagnetic simulations.

5 CONCLUSION

This study shows the possibility of studying primary remanence carriers from first principles by finite-element micromagnetic modelling. By individually modelling 302 silicate-hosted magnetite particles and comparing with single-crystal hysteresis measurements, we are able to show collectively and individually the source of stable remanence within these samples.

In orthopyroxene, magnetite exsolves as oblate particles elongated subparallel to the $[001]_{opx}$ direction. The summarized hysteresis have a dominant SD response that strongly contrasts with the single-crystal MD dominated hysteresis. By adding weighted fractions of MD hysteresis to the magnetic modelling, we managed to replicate the measured hysteresis with 1.6 per cent error. The MERRILL-calculated micromagnetics have contributed just 6 per cent to the hysteresis loop, but contributes 28 per cent to the remanent magnetization. The maximum M_{rs}/M_s, calculated magnetic susceptibility (χ^*) and the remanence direction is strongly correlated to elongation axes of magnetite and therefore the $[001]_{opx}$ direction. The maximum H_c is oriented in the $[100]_{opx}$ and parallel to the minimum χ^*, which reflects larger vortex nucleation fields when the applied field direction approaches the short axis. The maximum H_c is therefore orthogonal to the maximum M_{rs}/M_s, which is controlled by axis-aligned metastable single-domain states at zero field.

In plagioclase the magnetite exsolves as elongated needles that are primarily oriented in the $[001]_{plag}$ direction and those normal to the $(150)_{plag}$ and $(1\bar{5}0)_{plag}$ planes. The direction of magnetic remanence is in the direction of the magnetite population normal to the $(150)_{plag}$ and k_1 in the $[010]_{plag}$ direction. The maximum M_{rs}/M_s and maximum H_c align subparallel to the $[001]_{plag}$ indicating the primary remanence carriers are SD. The M_{rs}/M_s values of measured (0.4) and modelled (0.396) hysteresis curves differ only by 1 per cent, which we interpret to show that the remanent magnetization of micromagnetic models for plagioclase accurately represent the equilibrium magnetization of the bulk single crystal at its saturation remanence state. The surprisingly high H_c of the measured hysteresis loop can result from a variety of factors. The limited FIB interaction volume and pinning by natural imperfections, not included in the micromagnetic modelling, could explain the observed difference between the modelled (37 mT) and measured (65 mT) hysteresis loop.

These results provide the first statistically robust connection between micromagnetically modelled natural particle ensembles and bulk hysteresis measurements from the same samples. Small magnetite grain sizes are proportionally more important for remanent magnetization than for induced magnetization, and provide quantitative estimates of the two samples where FIB data are available. Our results, based on FIB, EBSD and MERRILL modelling indicate that the orthogonality relationship between the directions of maximal M_{rs}/M_s and maximal H_c may serve as an experimental indicator for the dominance of metastable SD particles as carriers of the remanent magnetization in single host crystals. The AMS of presumably paramagnetic single silicate crystals correlate suspiciously well with our calculations. This raises the question if the intended removal of ferromagnetic susceptibility from the measurement was really successful, even though a lattice aligned precipitation of ferrimagnetic particles could also by chance mimic the paramagnetic AMS. This study is the first of its kind, and it is important that future studies expand on these results to include a variety of silicates (micas, amphiboles, pyroxenes and plagioclase) and oxides (magnetite, ilmentite, ulvöspinel and hematite), thereby contributing to the understanding of magnetic particles from a fundamental perspective to the total magnetic hysteresis assemblage.

DATA AVAILABILITY

The summarized magnetic properties and individual particles shapes used in this paper are available in [dataverse], at https://doi.org/10.18710/AZT6UY [doi]. Further detailed micromagnetic simulations of individual grains in each external filed directions are available upon request, they are not in the database because of the substantial collective file sizes.

REFERENCES

Ageeva, O., Bian, G., Habler, G., Pertsev, A. & Abart, R., 2020. Crystallographic and shape orientations of magnetite micro-inclusions in plagioclase, *Contrib. Mineral. Petrol.,* **175**(10), 1–16.

Aharoni, A., 2000. *Introduction to the Theory of Ferromagnetism,* 2nd edn, Oxford Univ. Press.

Ayachit, U., 2015. *The Paraview Guide: A Parallel Visualization Application,* Kitware, Inc.

Bachmann, F., Hielscher, R. & Schaeben, H., 2010. Texture analysis with mtex–free and open source software toolbox, *Solid State Phenom.,* **160**, 63–68.

Biedermann, A.R., 2018. Magnetic anisotropy in single crystals: a review, *Geosciences,* **8**(8), 302.

Biedermann, A.R., Pettke, T., Angel, R.J. & Hirt, A.M., 2016. Anisotropy of magnetic susceptibility in alkali feldspar and plagioclase, *Geophys. Suppl. Mon. Not. R. Astron. Soc.,* **205**(1), 479–489.

Biedermann, A.R., Jackson, M., Chadima, M., Hirt, A.M. & Feinberg, J.M., 2020. Beyond the second-order magnetic anisotropy tensor: higher-order components due to oriented magnetite exsolutions in pyroxenes, and implications for palaeomagnetic and structural interpretations, *Geophys. J. Int.,* **223**(2), 915–933.

Bono, R.K., Tarduno, J.A., Nimmo, F. & Cottrell, R.D., 2019. Young inner core inferred from Ediacaran ultra-low geomagnetic field intensity, *Nat. Geosci.,* **12**(2), 143–147.

Buades, A., Coll, B. & Morel, J.-M., 2011. Non-local means denoising, *Image Process. On Line,* **1**, 208–212.

Burton-Johnson, A., Macpherson, C., Muraszko, J., Harrison, R. & Jordan, T.A., 2019. Tectonic strain recorded by magnetic fabrics (AMS) in Plutons, including Mt Kinabalu, Borneo: a tool to explore past tectonic regimes and syn-magmatic deformation, *J. Struct. Geol.,* **119**, 50–60.

Cawthorn, R., Cooper, G. & Webb, S., 1998. Connectivity between the western and eastern limbs of the Bushveld complex, *S. Afr. J. Geol.,* **101**(4), 291–298.

Cawthorn, R.G., Lundgaard, K.L., Tegner, C. & Wilson, J.R., 2016. Lateral variations in plagioclase compositions, main zone, Bushveld complex, South Africa: evidence for slow mixing of magmas in basinal structures, *Mineral. Mag.,* **80**(2), 213–225.

Champness, P. & Lorimer, G., 1974. A direct lattice-resolution study of precipitation (exsolution) in orthopyroxene, *Philos. Mag.,* **30**(2), 357–365.

Church, N.S., Feinberg, J.M. & Harrison, R.J., 2011. Low-temperature domain wall pinning in titanomagnetite: quantitative modeling of multidomain first-order reversal curve diagrams and AC susceptibility, *Geochem. Geophys. Geosyst.,* **12**(7), Q07Z27 , doi:10.1029/2011GC003538.

Crowson, P., 2001. *Minerals Handbook 2000-01: Statistics & Analyses of the World's Minerals Industry,* Mining Journal Books.

Darbon, J., Cunha, A., Chan, T.F., Osher, S. & Jensen, G.J., 2008. Fast nonlocal filtering applied to electron cryomicroscopy, in *Proceedings of the 2008 5th IEEE International Symposium on Biomedical Imaging: From Nano To Macro,* pp. 1331–1334, IEEE.

Davis, K.E., 1981. Magnetite rods in plagioclase as the primary carrier of stable NRM in ocean floor Gabbros, *Earth planet. Sci. Lett.,* **55**(1), 190–198.

Dawson-Haggerty *et al.*, 2019. Python library for loading and using triangular meshes. .trimesh.org

DeSimone, A., Kohn, R.V., Müller, S. & Otto, F., 2005. Recent analytical developments in micromagnetics, in *The Science of Hysteresis,* Vol. **II**, Chap. 4, pp. 269–381, eds Bertotti, G. & Mayergoyz, I., Elsevier.

Dieckmann, R., 1982. Defects and cation diffusion in magnetite (IV): nonstoichiometry and point defect structure of magnetite ($Fe_{3-\delta}O_4$), *Berichte der Bunsengesellschaft für physikalische Chemie,* **86**(2), 112–118.

Fabian, K. & Shcherbakov, V.P., 2018. Energy barriers in three-dimensional micromagnetic models and the physics of thermoviscous magnetization, *Geophys. J. Int.,* **215**(1), 314–324.

Feinberg, J.M., Wenk, H.-R., Renne, P.R. & Scott, G.R., 2004. Epitaxial relationships of clinopyroxene-hosted magnetite determined using electron backscatter diffraction (ebsd) technique, *Am. Mineral.,* **89**(2–3), 462–466.

Feinberg, J.M., Scott, G.R., Renne, P.R. & Wenk, H.-R., 2005. Exsolved magnetite inclusions in silicates: Features determining their remanence behavior, *Geology,* **33**(6), 513–516.

Feinberg, J.M., Wenk, H.-R., Scott, G.R. & Renne, P.R., 2006. Preferred orientation and anisotropy of seismic and magnetic properties in Gabbronorites from the bushveld layered intrusion, *Tectonophysics,* **420**(3–4), 345–356.

Fleet, M., Bilcox, G.A. & Barnett, R.L., 1980. Oriented magnetite inclusions in pyroxenes from the Grenville Province, *Can. Mineral.,* **18**(1), 89–99.

Frandsen, C., Stipp, S., McEnroe, S., Madsen, M. & Knudsen, J., 2004. Magnetic domain structures and stray fields of individual elongated magnetite grains revealed by magnetic force microscopy (MFM), *Phys. Earth planet. Inter.,* **141**(2), 121–129.

Hattingh, P., 1986. The palaeomagnetism of the main zone of the eastern Bushveld complex, *Tectonophysics,* **124**(3–4), 271–295.

Heider, F., Zitzelsberger, A. & Fabian, K., 1996. Magnetic susceptibility and remanent coercive force in grown magnetite crystals from 0.1 μm to 6 mm, *Phys. Earth planet. Inter.,* **93**(3–4), 239–256.

Hirt, A.M. & Biedermann, A.R., 2019. Preferred orientation of ferromagnetic phases in rock-forming minerals: insights from magnetic anisotropy of single crystals, *Can. J. Earth Sci.,* **56**(9), 994–1001.

Kirby, S. & Etheridge, M., 1981. Exsolution of Ca-clinopyroxene from orthopyroxene aided by deformation, *Phys. Chem. Miner.,* **7**(3), 105–109.

Krasa, D., Heunemann, C., Leonhardt, R. & Petersen, N., 2003. Experimental procedure to detect multidomain remanence during Thellier-Thellier experiments, *Phys. Chem. Earth,* **28**(16–19), 681–687.

Lawson, C.L. & Hanson, R.J., 1995. *Solving Least Squares Problems,* SIAM.

Letts, S., Torsvik, T.H., Webb, S.J. & Ashwal, L.D., 2009. Palaeomagnetism of the 2054 Ma Bushveld complex (South Africa): implications for emplacement and cooling, *Geophys. J. Int.,* **179**(2), 850–872.

Lundgaard, K.L., 2003. *Magma Chamber Processes Studied in Two Layered Instrusions [including 4 Papers],* Department of Earth Sciences, Aarhus University.

Lundgaard, K.L., Tegner, C., Cawthorn, R.G., Kruger, F.J. & Wilson, J.R., 2006. Trapped intercumulus liquid in the main zone of the eastern Bushveld complex, South Africa, *Contrib. Mineral. Petrol.,* **151**(3), 352–369.

Martín-Hernández, F. & Ferré, E.C., 2007. Separation of paramagnetic and ferrimagnetic anisotropies: a review, *J. geophys. Res.,* **112**(B3), doi:10.1029/2006JB004340.

McEnroe, S., Skilbrei, J., Robinson, P., Heidelbach, F., Langenhorst, F. & Brown, L., 2004. Magnetic anomalies, layered intrusions and Mars, *Geophys. Res. Lett.,* **31**(19),.

Nikolaisen, E.S., Harrison, R., Fabian, K. & McEnroe, S.A., 2020. Hysteresis of natural magnetite ensembles: micromagnetics of silicate-hosted magnetite inclusions based on focused-ion-beam nanotomography, *Geochem. Geophys. Geosyst.,* **21**(11),.

Ó Conbhuí, P., Williams, W., Fabian, K., Ridley, P., Nagy, L. & Muxworthy, A.R., 2018. MERRILL: micromagnetic Earth related robust interpreted language laboratory, *Geochem. Geophys. Geosyst.,* **19** , doi:10.1002/2017gc007279.

Pastore, Z., Church, N.S. & McEnroe, S.A., 2019. Multistep parametric inversion of scanning magnetic microscopy data for modeling magnetization of multidomain magnetite, *Geochem. Geophys. Geosyst.,* **20**(11), 5334–5351.

Reiche, M. & Bautsch, H.-J., 1985. Electron microscopical study of garnet exsolution in orthopyroxene, *Phys. Chem. Miner.,* **12**(1), 29–33.

Renne, P.R., Scott, G.R., Glen, J.M. & Feinberg, J.M., 2002. Oriented inclusions of magnetite in clinopyroxene: source of stable remanent magnetization in Gabbros of the Messum complex, Namibia, *Geochem. Geophys. Geosyst.,* **3**(12), 1–11.

Richter, C. & van der Pluijm, B.A., 1994. Separation of paramagnetic and ferrimagnetic susceptibilities using low temperature magnetic susceptibilities and comparison with high field methods, *Phys. Earth planet. Inter.,* **82**(2), 113–123.

Scoates, J.S., Wall, C.J., Friedman, R.M., Weis, D., Mathez, E.A. & VanTongeren, J.A., 2021. Dating the Bushveld complex: timing of crystallization, duration of magmatism, and cooling of the world's largest layered intrusion and related rocks, *J. Petrol.,* **62**(2),.

Sobolev, P., 1990. Orientation of acicular iron-ore mineral inclusions in plagioclase, *Int. Geol. Rev.,* **32**(6), 616–628.

Sørensen, B.E., Hjelen, J., Ånes, H.W. & Breivik, T., 2020. Recent features in EBSD, including new trapezoidal correction for multi-mapping, *IOP Conf. Ser.: Mater. Sci. Eng.,* **891,** 012021 , doi:10.1088/1757-899x/891/1/012021.

Stacey, F.D. & Banerjee, S.K., 1974. *The Physical Principles of Rock Magnetism,* Elsevier.

Suuronen, J.-P. & Sayab, M., 2018. 3D Nanopetrography and chemical imaging of datable zircons by synchrotron multimodal X-ray tomography, *Scient. Rep.,* **8**(1), 1–13.

Tegner, C. & Cawthorn, R.G., 2010. Iron in plagioclase in the Bushveld and Skaergaard intrusions: implications for iron contents in evolving basic magmas, *Contrib. Mineral. Petrol.,* **159**(5), 719–730.

Thormann, L., Buchspies, B., Mbohwa, C. & Kaltschmitt, M., 2017. PGE production in southern Africa, part I: production and market trends, *Minerals,* **7**(11), 224.

Usui, Y., Shibuya, T., Sawaki, Y. & Komiya, T., 2015. Rock magnetism of tiny exsolved magnetite in plagioclase from a Paleoarchean granitoid in the Pilbara Craton, *Geochem. Geophys. Geosyst.,* **16**(1), 112–125.

Wager, L.R. & Brown, G.M., 1967. *Layered Igneous Rocks,* WH Freeman.

Webb, S.J., Ashwal, L.D. & Cawthorn, R.G., 2011. Continuity between eastern and western Bushveld complex, South Africa, confirmed by xenoliths from kimberlite, *Contrib. Mineral. Petrol.,* **162**(1), 101–107.

SUPPORTING INFORMATION

Supplementary data are available at *GJI* online.

Please note: Oxford University Press is not responsible for the content or functionality of any supporting materials supplied by the authors. Any queries (other than missing material) should be directed to the corresponding author for the paper.

APPENDIX

The here used list of approximately equi-distributed Fibonacci directions on the upper hemisphere $z > 0$ can be calculated in Mathematica by

```
FN = 20;
XYZ[lon_, lat_] := {Cos[lon] Cos[lat], Sin[lon]
Cos[lat],Sin[lat]};
Table[XYZ[2 Pi k/ GoldenRatio , ArcSin
[2 k/(2 FN + 1)]], {k, 1., FN}]
```

External field direction locations
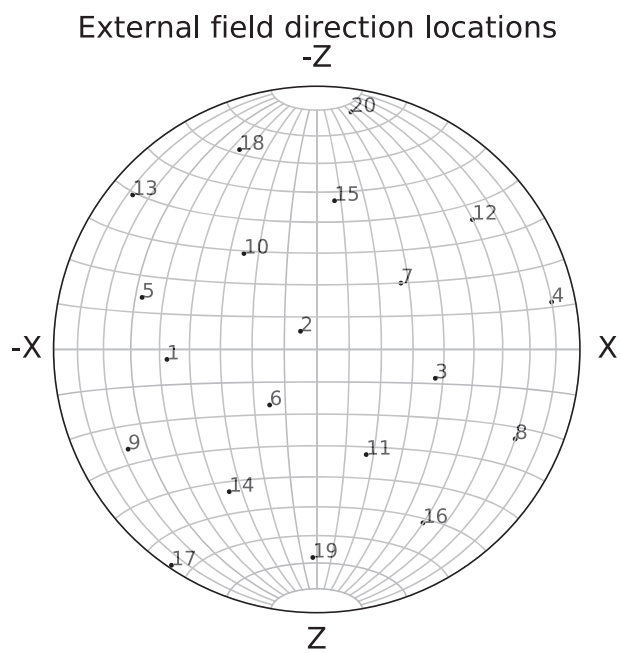
Figure A1. Stereographic projection showing the location for each external field directions as seen in Fig. 8.

Table A1. The remanence vector directions of each silicate for the 20 applied external field directions (labelled in Fig. 9a for orthopyroxene and 9 b for plagioclase) during MERRILL modelling. The following matrix show the conversion of axes between the figures (Py) and the calculations in MERRILL, where the axes in MERRILL = mesh = FIB.

$$\begin{pmatrix} X_{Py} \\ Y_{Py} \\ Z_{Py} \end{pmatrix} = \begin{pmatrix} 1 & 0 & 0 \\ 0 & 0 & 1 \\ 0 & -1 & 0 \end{pmatrix} \begin{pmatrix} X_{Merr} \\ Y_{Merr} \\ Z_{Merr} \end{pmatrix}$$

Direction	External field			Orthopyroxene			Plagioclase		
	FIB_X	FIB_Y	FIB_Z	FIB_{MX}	FIB_{MY}	FIB_{MZ}	FIB_{MX}	FIB_{MY}	FIB_{MZ}
1	− 0.736	− 0.675	0.049	− 0.346	− 0.562	0.359	− 0.306	− 0.382	0.027
2	0.087	0.99	0.097	− 0.108	0.026	− 0.002	− 0.082	0.044	0.022
3	0.602	− 0.785	0.146	− 0.020	− 0.180	0.104	0.058	− 0.100	− 0.053
4	− 0.965	0.171	0.195	− 0.105	− 0.146	0.100	− 0.047	0.014	0.161
5	0.818	0.521	0.244	− 0.015	− 0.005	0.008	0.024	0.088	0.012
6	− 0.248	− 0.923	0.293	− 0.067	− 0.098	0.067	− 0.022	0.004	0.016
7	− 0.433	0.834	0.341	− 0.081	0.001	0.012	− 0.065	0.061	0.050
8	0.864	− 0.316	0.390	− 0.049	− 0.072	0.049	− 0.012	0.008	0.023
9	− 0.831	− 0.343	0.439	− 0.082	− 0.127	0.084	− 0.046	− 0.031	0.029
10	0.369	0.790	0.488	− 0.038	− 0.057	0.039	− 0.028	0.009	0.047
11	0.253	− 0.805	0.537	− 0.024	− 0.109	0.066	− 0.011	− 0.031	0.046
12	− 0.701	0.406	0.585	− 0.048	− 0.085	0.056	− 0.038	0.003	0.064
13	0.755	0.166	0.634	− 0.029	− 0.118	0.073	− 0.020	0.026	0.075
14	− 0.420	− 0.596	0.683	− 0.053	− 0.151	0.094	− 0.039	− 0.001	0.076
15	− 0.087	0.676	0.732	− 0.060	− 0.102	0.067	− 0.055	0.026	0.090
16	0.478	− 0.403	0.780	− 0.046	− 0.132	0.083	− 0.039	− 0.0004	0.088
17	− 0.558	− 0.023	0.829	− 0.064	− 0.158	0.099	− 0.058	0.018	0.099
18	0.339	0.337	0.878	− 0.050	− 0.171	0.106	− 0.048	0.037	0.107
19	− 0.017	− 0.375	0.927	− 0.059	− 0.193	0.119	− 0.053	0.015	0.108
20	− 0.141	0.168	0.975	− 0.074	− 0.211	0.132	− 0.642	0.034	0.117

Table A2. The total hysteresis properties calculated by summarizing the individual hysteresis loops for all particles in each external field directions visualized for plagioclase in Fig. 5(a) and for orthopyroxene in Fig. 5(b).

| Direction	Orthopyroxene			Plagioclase		
	M_{rs}/M_s	H_c (mT)	χ^* (SI)	M_{rs}/M_s	H_c (mT)	χ^* (SI)
1	0.616	15.692	15.4	0.445	34.569	4.1
2	0.561	22.228	8.4	0.392	41.164	4.2
3	0.548	15.029	16.6	0.325	34.363	3.8
4	0.380	9.562	15.3	0.372	28.063	4.9
5	0.452	15.592	12.3	0.371	31.121	4.0
6	0.709	17.448	14.9	0.454	45.037	4.0
7	0.407	18.847	9.68	0.477	40.971	4.4
8	0.413	12.412	15.8	0.198	23.342	3.6
9	0.603	13.659	17.6	0.412	25.873	5.8
10	0.338	28.743	4.5	0.392	35.929	4.3
11	0.684	17.030	14.7	0.371	46.593	3.5
12	0.284	10.143	10.9	0.510	29.970	5.1
13	0.231	13.722	9.0	0.236	22.394	4.3
14	0.725	17.553	14.7	0.453	30.647	4.7
15	0.153	32.254	2.7	0.518	39.469	4.5
16	0.516	17.993	12.2	0.272	30.492	3.3
17	0.484	18.105	10.2	0.464	24.328	5.5
18	0.132	27.471	2.7	0.416	35.198	4.7
19	0.565	21.852	8.9	0.362	29.469	4.6
20	0.304	33.737	3.5	0.488	31.278	5.2

Reflected light microscopy in oil at 125X
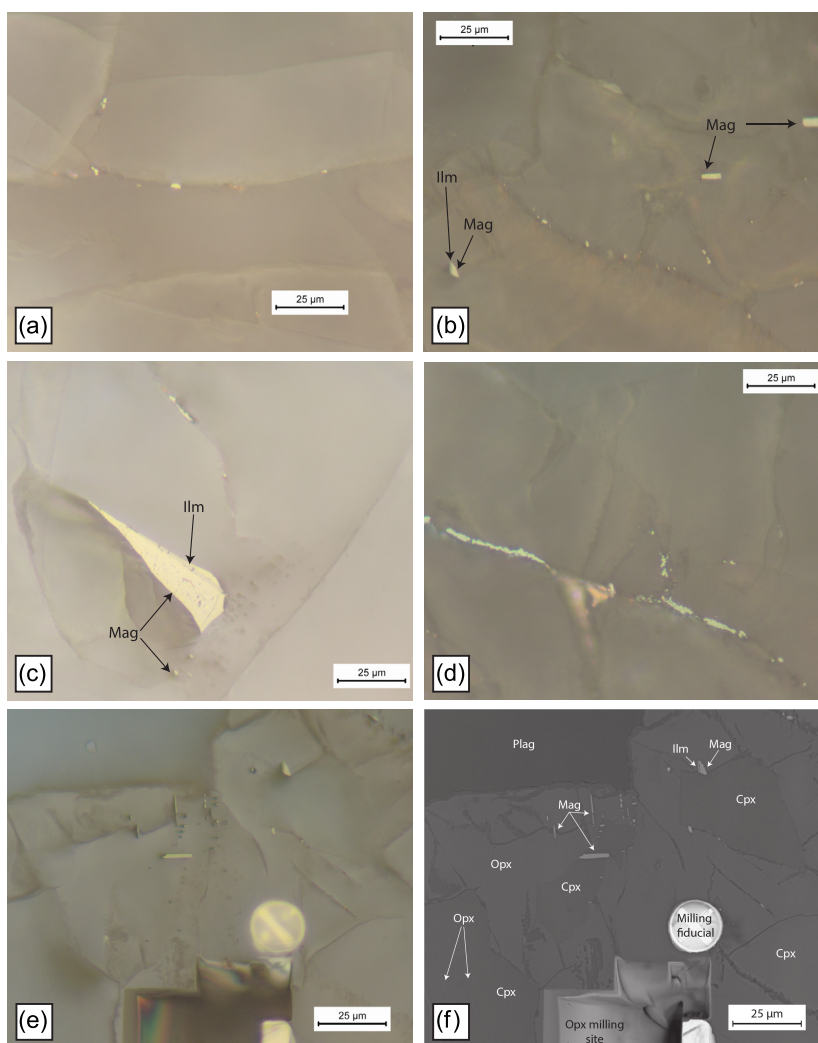
Figure A2. Optical images taken at 125 × in oil. (a) Grain boundary Fe-oxides, (b) magnetite crystallographic inclusions with ilmenite lamellae and grain boundary Fe-oxides. (c) large crystallographic oriented magnetite inclusion with ilmenite lamellae next to magnetite lamellae. (d) crack filling Fe-oxides with carbonate in the orthopyroxene. (e) patch of magnetite lamellae intersected by the milled orthopyroxene volume (Figs 1c and 3). (f) BSD of the same location as in (e), showing the clinopyroxene exsolution and the shape differences of the magnetite when hosted by different pyroxenes.
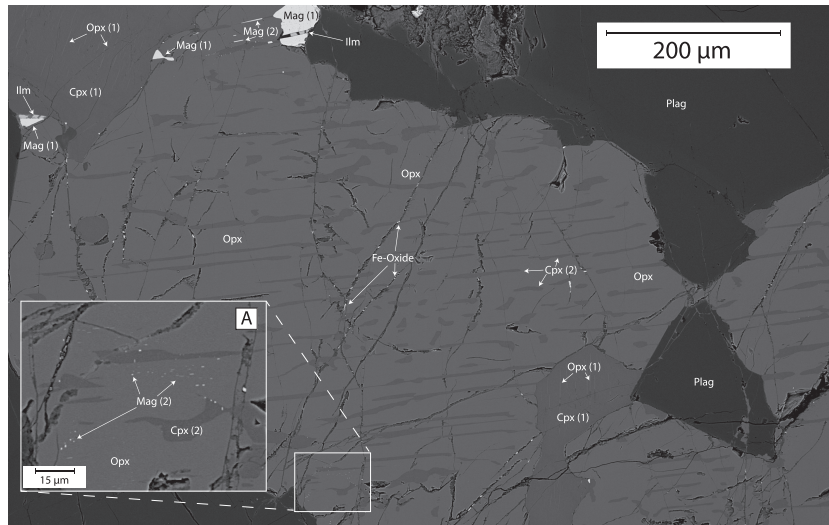
Figure A3. BSD image of the general pyroxene crystals, dominated by orthopyroxene (Opx). The orthopyroxene contain discrete clinopyroxene crystals (Cpx) and esxolution lamellae (In-Pig) of inverted pigeonite. The discrete clinopyroxene crystals have exsolution lamellae of orthopyroxene (Opx(1)) and Al-spinel. Magnetite (Mag(1)) are observed as crystallographic oriented inclusions ($50-100$ μm) with ilmenite lamellae (Ilm), as exsolution lamellae (Mag 2) and grain boundary inclusions (Fig. A2a and b). Fe-oxides occur as crack infill (Fe-Oxide and Fig. A2d).
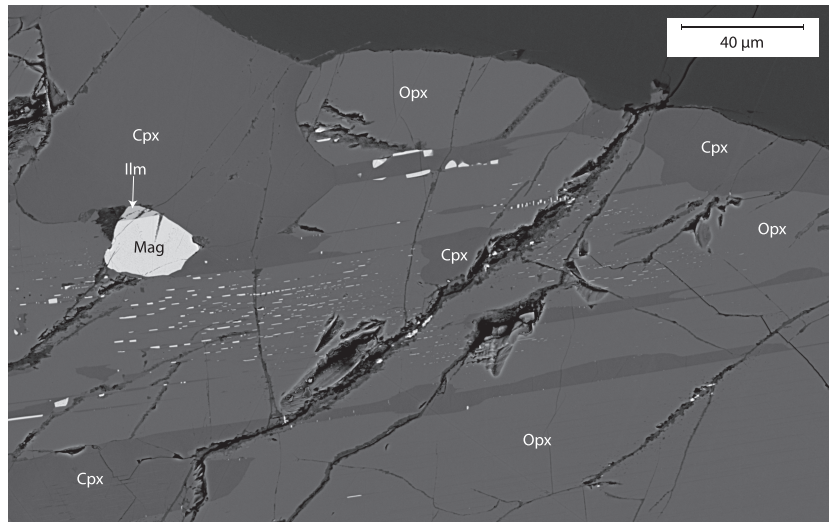
Figure A4. Patch of concentrated magnetite lamellae oriented in the [001]$_{opx}$ direction.
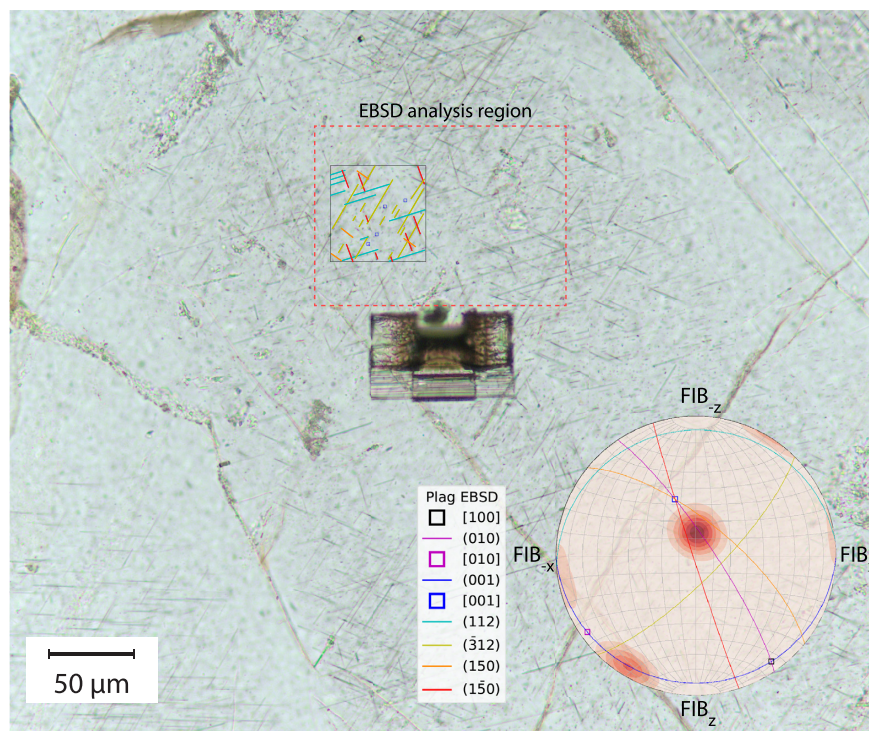
Figure A5. Optical image of the milling site in the plagioclase with overlay of the EBSD stereonet. Each documented direction of magnetite exsolutions from other publications that we observed are indicated with a line in the same colour as the crystallographic orientation the magnetite is expected to populate. The magnetite exsolutions that are subparallel to the $[001]_{plag}$ is indicated at the centre of the blue squares. The red contours show the population of elongation axes from the milling volume (Fig. 2).
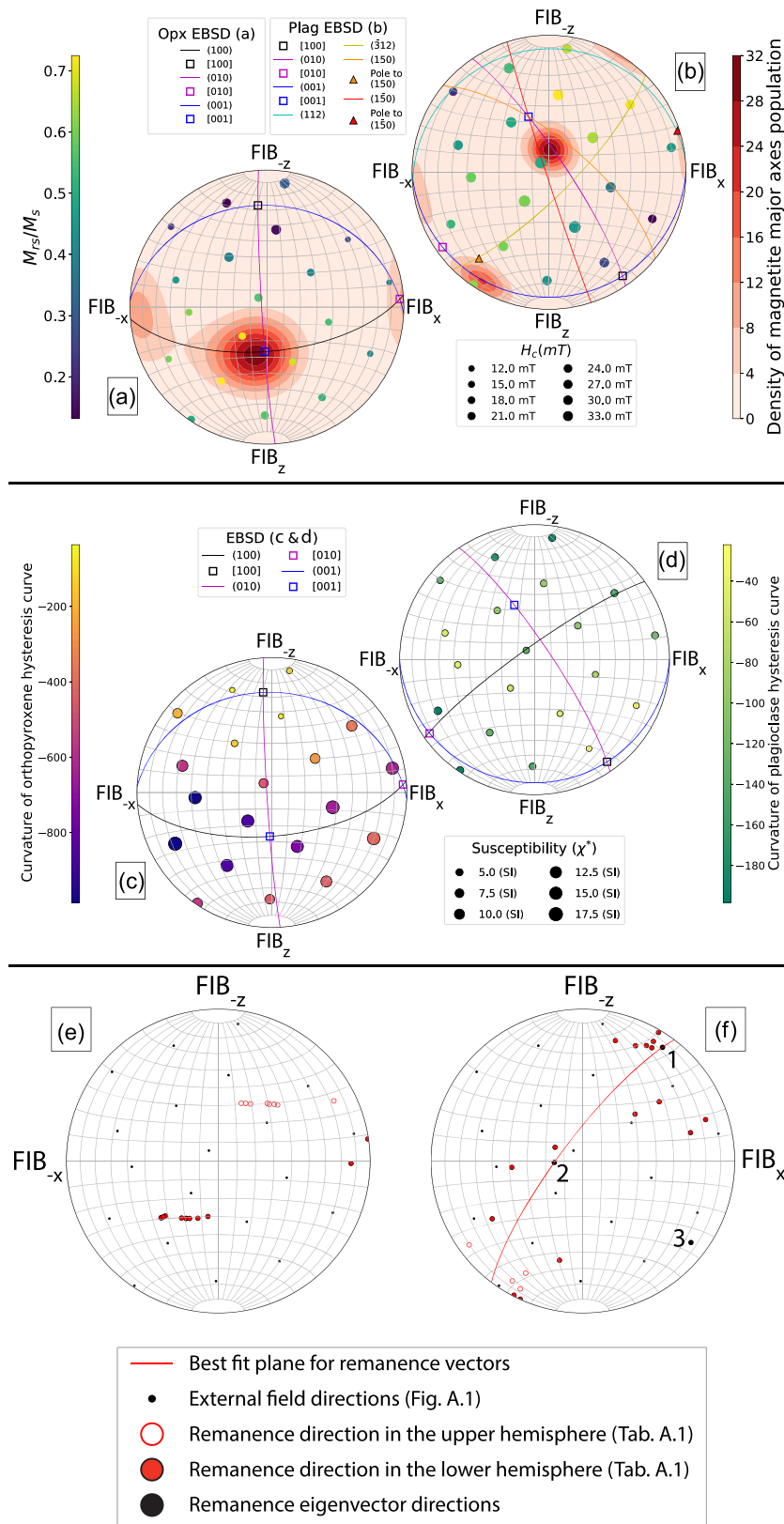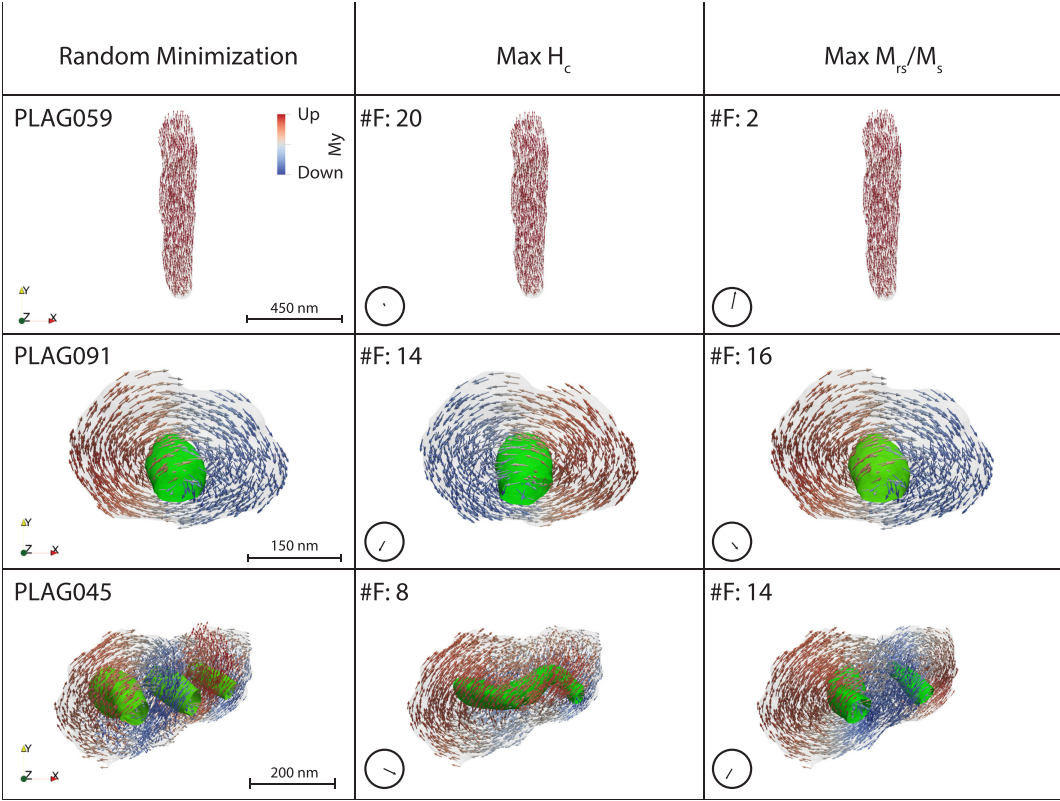
Figure A6. A single collective figure of Figs 8, 9 and 10.

Figure A7. Figure of micromagnetic models of the different domain states in plagioclase. The random minimization state (left-hand column) is the lowest of 20 minimizations started from a random seed. The maximum H_c (middle column) and ma M_{rs}/M_s (right-hand column) states are saturation remanence states calculated from the hysteresis loops for individual external field direction (#F) that yielded the maximum coercivity and saturation magnetization, respectively (Fig. A1). The FIB$_x$ and FIB$_y$ direction of #F is visually represented as a stereographic projection of the upper hemisphere, for each particle by the arrow at the bottom left corner. All external fields have a positive FIB$_z$ direction oriented out of the page.